Article

SOURCE DATA | TRANSPARENT PROCESS | OPEN ACCESS

EMBO reports

Centrosome linker protein C-Nap1 maintains stem cells in mouse testes

Hairuo Dang[1,2], Ana Martin-Villalba[3] & Elmar Schiebel[1,*]

Abstract

The centrosome linker component C-Nap1 (encoded by *CEP250*) anchors filaments to centrioles that provide centrosome cohesion by connecting the two centrosomes of an interphase cell into a single microtubule organizing unit. The role of the centrosome linker during development of an animal remains enigmatic. Here, we show that male *CEP250*$^{-/-}$ mice are sterile because sperm production is abolished. Premature centrosome separation means that germ stem cells in *CEP250*$^{-/-}$ mice fail to establish an E-cadherin polarity mark and are unable to maintain the older mother centrosome on the basal site of the seminiferous tubules. This failure prompts premature stem cell differentiation in expense of germ stem cell expansion. The concomitant induction of apoptosis triggers the complete depletion of germ stem cells and consequently infertility. Our study reveals a role for centrosome cohesion in asymmetric cell division, stem cell maintenance, and fertility.

Keywords apoptosis; centrosome; C-Nap1; development; stem cell
Subject Categories Cell Adhesion, Polarity & Cytoskeleton; Stem Cells & Regenerative Medicine
DOI 10.15252/embr.202153805 | Received 13 August 2021 | Revised 13 April 2022 | Accepted 27 April 2022 | Published online 23 May 2022
EMBO Reports (2022) 23: e53805

Introduction

The centrosome is the main microtubule organizing center (MTOC) in animal cells. It controls shape, polarity, and motility of cells and organizes the two spindle poles of the mitotic spindle (Conduit *et al*, 2015). The centrosome consists of centrioles of nine microtubule triplets and the surrounding pericentriolar material (PCM; Bornens, 2002). The centriole provides structural integrity to the centrosomes and together with some PCM proteins enables the centrosome to duplicate once per cell cycle by a scaffold-based mechanism (Tsou & Stearns, 2006). PCM proteins participate in microtubule nucleation and anchoring, and support cell cycle-dependent centrosome duplication. The two centrioles of a G1 cell duplicate in G1/S phase by a semi-conservative mechanism followed by daughter centriole maturation that is stretched over one and a half cell cycles. Therefore, the two G1 phase centrioles/centrosomes are distinct with respect to age and structure. Only the older, mother, centriole carries distal (DA) and subdistal appendages (SDA). The daughter centriole gains these structures after cells have completed the ensuing mitosis. The DAs of the mother centriole are essential for the docking of the centriole to the plasma membrane and the formation of a primary cilium, a signaling, and sensing organelle of cells (Delgehyr *et al*, 2005; Graser *et al*, 2007; Tanos *et al*, 2013). The SDAs stably bind microtubules that interact with PCM organized microtubules of the daughter centrosome to spatially organize both centrosomes (Hata *et al*, 2019).

Another centrosome substructure is the centrosome linker, a proteinaceous array of filaments that includes the proteins rootletin and CEP68. These linker proteins connect the two centrioles into one microtubule organizing center by binding to the anchoring protein C-Nap1 (encoded by *CEP250*) located at the proximal end of centrioles. This centrosome linker persists until the end of G2/early mitosis when the kinase NEK2 dissolves the linker through phosphorylation to enable the two centrosomes to organize the spindle poles of the mitotic spindle (Fry *et al*, 1998; Bahe *et al*, 2005; Remo *et al*, 2020). Centrosome cohesion is also supported by the parallel microtubule pathway mentioned above (Hata *et al*, 2019).

The essential functions in mitosis and ciliogenesis mean that the centrosome plays important roles in maintaining human health. Defects in centrosome function are correlated with several diseases such as cancer, microcephaly, primordial dwarfism, and ciliopathies (Chan, 2011; Nechipurenko *et al*, 2016; Nigg & Holland, 2018; Fabbri *et al*, 2019; Lens & Medema, 2019; Shaheen *et al*, 2019). Consistently, recent studies have highlighted a strong reliance upon centrosome function in development. Centrosomes control the asymmetric division of neuronal stem cells (NSCs) and germ stem cells (GSCs) in *Drosophila*, partly as a consequence of asymmetric behavior of the two centrosomes (Yamashita *et al*, 2007). This role in NSCs and GSCs fate resonates with the role played by asymmetric centriole inheritance in the developing mammalian brain (Chavali *et al*, 2014; Nigg & Holland, 2018). After cell division, the mother centriole assembles cilia earlier than the daughter, which probably functions as the signal for stem cell maintenance (Paridaen *et al*, 2013). However, whether centrosomes have a general role in mammalian stem cell division and whether there is conservation of the mechanisms and the molecules involved in such processes remains to be determined.

1 Zentrum für Molekulare Biologie der Universität Heidelberg, Deutsches Krebsforschungszentrum-ZMBH Allianz, Universität Heidelberg, Heidelberg, Germany
2 Heidelberg Biosciences International Graduate School (HBIGS), Universität Heidelberg, Heidelberg, Germany
3 Deutsches Krebsforschungszentrum-ZMBH Allianz, Universität Heidelberg, Heidelberg, Germany
*Corresponding author. Tel: +49 6221 54 6814; E-mail: e.schiebel@zmbh.uni-heidelberg.de

While the essential functions of centrosomes as microtubule organizers and the role of centriole appendages in ciliogenesis at the cellular level and in a developing organism are well established, the role of the centrosome linker is more enigmatic. Knockout of *CEP250* in the non-transformed RPE1 cells (hTERT-immortalized retinal pigment epithelial cells) are completely devoid of centrosome linker function and exhibit only mild defects upon cell migration and Golgi organization (Panic *et al*, 2015). Interestingly, a *CEP250* mutation in cattle was connected to smaller brain size and stature (Floriot *et al*, 2015). However, the reason for this developmental defect and the question as to whether it is caused by the *CEP250* mutation alone remains to be explored. Thus, the role of the centrosome linker in the context of an organism is largely unclear.

Here, we began by asking what are the consequences of the loss of the centrosome linker by characterizing the phenotypes of a *CEP*250$^{-/-}$ mouse. Loss of *CEP250* did not reduce brain or body size, nor did it seem to have significant impact on the structure and organization of most organs. However, we found that the function of the reproductive organs, particularly the testis, was severely impaired in the *CEP250*$^{-/-}$ mice, leading to complete infertility in male mice. We discovered that the centrosome linker ensures centrosome cohesion until G2/prophase in *CEP250*$^{+/+}$ but not in *CEP250*$^{-/-}$ testis. Premature centrosome separation in *CEP*250$^{-/-}$ mice led to incorrect positioning of the older centrosome and a failure to establish the E-cadherin polarity mark. These centrosome deficiencies, in turn, led to premature differentiation of the male germ stem cells (GSCs) that are the key for male spermatogenesis (de Rooij, 2017), accompanied by their complete depletion. These findings define a novel function of the centrosome linker and centrosomes in male GSC division.

Results

CEP250 null mice show defects in reproductive organs with large reduction of germ cells (GCs), leading to decreased fertility in males and females

In order to determine the function of the centrosome linker at the level of the entire organism, we deleted the *CEP250* gene by crossing *CEP250*$^{flox/flox}$ mice with whole-body Cre mice to generate a *CEP250*$^{-/-}$ mouse (Fig EV1A). Deletion of exons 6–7 in *CEP250*$^{-/-}$ mice leads to a predicted N-terminal C-Nap1 fragment of 184 amino acids that does not bind to centrosomes and has no obvious function (Panic *et al*, 2015) (Fig EV1B). We confirmed the genomic deletion and the loss of the C-Nap1 protein in tissue samples (Fig EV1C–F) and observed significant increase in centrosome separation in tissue samples from 1 to 3 μm (Fig EV1G). In addition, the average inter-centrosomal distance was increased from 0.5 μm in wild-type *CEP250*$^{+/+}$ mouse embryonic fibroblasts (MEFs) to 5 μm in *CEP250*$^{-/-}$ MEFs (Fig EV1H and I). This impact upon centrosome cohesion was further increased in *CEP250*$^{-/-}$ MEFs by microtubule depolymerization with the drug nocodazole to inactive the microtubule-dependent centrosome cohesion pathway (Fig EV1H and J; Hata *et al*, 2019). Thus, deletion of *CEP250* impairs the function of the centrosome linker in mouse.

Centrosome defects have been tightly linked to brain malformations. We therefore assessed the body and brain weight of *CEP250* null mice, but found no significant reduction in either (Fig 1A–D). Furthermore, histologically examination of most organs failed to reveal major abnormalities (Appendix Fig S1A–H). However, we did detect a striking reduction of the adult male reproductive tract including a greater than 80% reduction in testis size in *CEP250*$^{-/-}$ mice (Fig 1E–G). The female *CEP250*$^{-/-}$ mice also displayed > 20% reduction in ovary weight (Appendix Fig S1I–K). As a consequence, mating *CEP250*$^{-/-}$ male mice with *CEP250*$^{+/+}$ female failed to produce any offspring, indicating sterility of male *CEP250*$^{-/-}$ mice (Fig 1H). The *CEP250*$^{-/-}$ females mated with *CEP250*$^{+/+}$ males showed a 50% reduction in litter size, to reveal hypo-fertility in females (Fig 1H).

The testis generates sperm for more or less the entire life span of a male. This requires high coordination between germ stem cell self-expansion and differentiation (Griswold, 2016). These development steps take place in the seminiferous tubules (STs) of the testis that has a defined structural architecture. Undifferentiated spermatogonia localize at, or close to, the basement membrane of the STs and translocate toward the lumen of the STs (Oatley & Brinster, 2012). Examinations of adult testes (14 weeks after birth) cross-sections of *CEP250*$^{-/-}$ mice revealed abnormalities in this organization and sperm production (Fig 1I–L). *CEP250*$^{-/-}$ mice also display fewer number and smaller size of STs as compared to the *CEP250*$^{+/+}$ (Appendix Fig S2A and B). *CEP250*$^{-/-}$ STs displayed decrease cellularity as well as loss of normal organization of spermatogenic cells (Fig 1I). Histological examination of *CEP250*$^{-/-}$ caput and caudal epididymis revealed lack of spermatozoa (Fig 1J). While in *CEP250*$^{+/+}$ mice an average approx. 60 million viable sperms per mouse at any one time were counted, the epididymis of *CEP250*$^{-/-}$ mice were completely devoid of sperms (Fig 1K and L). Thereafter, we asked whether germ cells are maintained in the seminiferous tubules of adult testes by immunostaining to detect Mouse Vasa Homologue (MVH), a marker for both male and female mouse germ cells, including all spermatogenic cells at this stage (Tanaka *et al*, 2000; McClellan *et al*, 2003; Song *et al*, 2016). A drastic reduction of germ cells was observed in adult *CEP250*$^{-/-}$ testes (14 weeks) with almost no spermatogenic cells being detected (Fig 1M). This reduction of germ cells was also observed in *CEP250*$^{-/-}$ female adult ovaries, where the germ cell number was significantly reduced (Appendix Fig S1L and M). Thus, *CEP250*$^{-/-}$ mice show strong defects in the development of the reproductive organs, which is particularly pronounced in the testis.

Testis defects associated with *CEP250* loss is germ cell specific

Spermatogenesis defects may either be germ cell-intrinsic, or arise from defective interactions of spermatogenic cells with supporting cells, e.g., Sertoli cells (Griswold, 1998; Yokonishi *et al*, 2020). We examined Sertoli cells using the GATA Binding Protein 4 (GATA4) as marker (Chen *et al*, 2015). The population of Sertoli cells at the basement membrane of the seminiferous tubules in adult *CEP250*$^{-/-}$ testes (14 weeks) was comparable to the same population in *CEP250*$^{+/+}$ mice (Fig 1N). In addition, the number of the Sertoli cells in *CEP250*$^{-/-}$ mice, normalized to the tubule size, showed no significantly deviation from that noted in *CEP250*$^{+/+}$ (Fig 1O). Together, this strongly suggests that the defects in *CEP250*$^{-/-}$ mice may arise from a direct impact upon germ cells rather than an indirect consequence of compromised function of Sertoli cells.

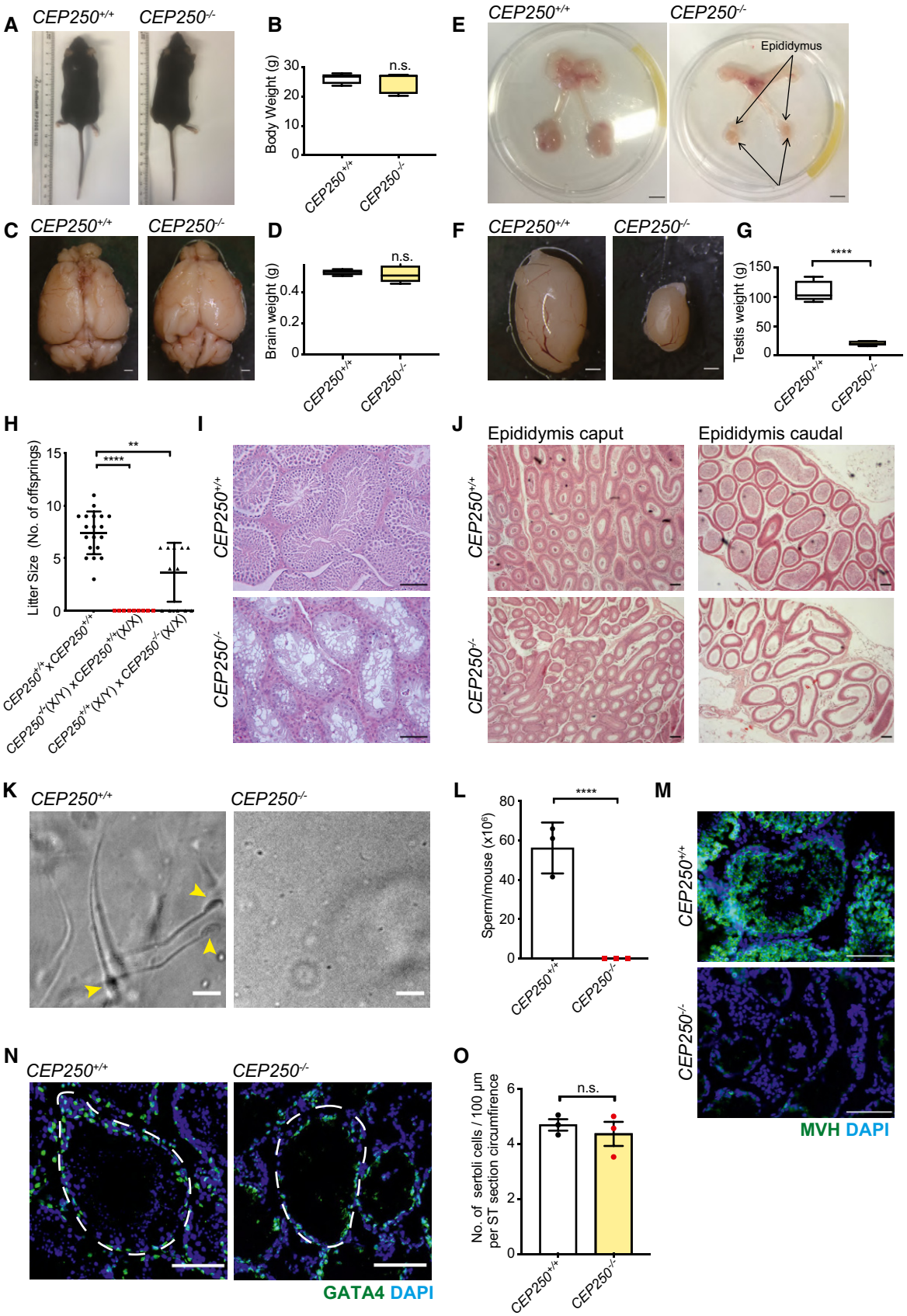
A
CEP250+/+
CEP250-/-
B
Body Weight (g)
n.s.
E
Epididymus
C
D
Brain weight (g)
F
G
Testis weight (g)
****
H
Litter Size (No. of offsprings)
**
****
I
J
Epididymis caput
Epididymis caudal
K
L
Sperm/mouse (x10⁶)
M
MVH DAPI
N
GATA4 DAPI
O
No. of sertoli cells / 100 µm per ST section circumfirence

Figure 1.

Figure 1. *CEP250* null mice show defect in germ line development in the testes and ovaries.

A Size of adult (9- to 14-week-old) *CEP250*$^{+/+}$ and *CEP250*$^{-/-}$ mice.
B Body weight of *CEP250*$^{+/+}$ and *CEP250*$^{-/-}$ mice (9- to 14-week-old). *CEP250*$^{+/+}$ $n = 5$ mice, *CEP250*$^{-/-}$ $n = 5$ mice.
C Brains from adult *CEP250*$^{+/+}$ and *CEP250*$^{-/-}$ mice (9- to 14-week-old). Scale bars: 1000 μm.
D Brain weight of 9- to 14-week-old mice. *CEP250*$^{+/+}$ $n = 5$ mice, *CEP250*$^{-/-}$ $n = 5$ mice.
E Adult male reproductive tract (9- to 14-week-old) *CEP250*$^{+/+}$ and *CEP250*$^{-/-}$.
F Adult testis (9- to 14-week-old) of *CEP250*$^{+/+}$ and *CEP250*$^{-/-}$ mice. Scale bars: 1000 μm.
G Adult testis (9- to 14-week-old) weight of *CEP250*$^{+/+}$ and *CEP250*$^{-/-}$ mice. *CEP250*$^{+/+}$ $n = 10$ mice, *CEP250*$^{-/-}$ $n = 10$ mice.
H Litter size (denoted by average number of offspring/litter) produced by mating pairs of the indicated genotypes of mice (9- to 14-week-old). Mating pairs, *CEP250*$^{+/+}$ x *CEP250*$^{+/+}$ $n = 19$, *CEP250*$^{-/-}$ (male) x *CEP250*$^{+/+}$ (female) $n = 9$ matings, *CEP250*$^{-/-}$ (female) x *CEP250*$^{+/+}$ (male) $n = 12$ matings.
I "H and E staining" of adult testis (9- to 14-week-old). Cross-sections of *CEP250*$^{+/+}$ and *CEP250*$^{-/-}$ testes are shown. Scale bars: 100 μm.
J "H and E staining" of adult (9- to 14-week-old) epididymis caput (left) and epididymis caudal (right) cross-sections *CEP250*$^{+/+}$ and *CEP250*$^{-/-}$ mice. Scale bars: 100 μm.
K Bright-field image of live epididymal sperm from *CEP250*$^{+/+}$ and *CEP250*$^{-/-}$ mice (9- to 14-week-old). Scale bars: 10 μm. Arrow heads highlight the sperm heads.
L Quantification of (K), sperm number per mouse. *CEP250*$^{+/+}$ $n = 3$ mice, *CEP250*$^{-/-}$ $n = 3$ mice.
M Immunofluorescence for MVH (green) with DAPI staining (blue) of 10-μm testis cryo-sections from adult *CEP250*$^{+/+}$ and *CEP250*$^{-/-}$ mice (9- to 14-week-old). In *CEP250*$^{+/+}$, numerous MVH+ cells were detected in the seminiferous tubules, whereas *CEP250*$^{-/-}$ seminiferous tubules lacked MVH+ germ cells. Scale bars: 100 μm.
N Immunofluorescence for GATA4 (green) with DAPI staining (blue) of 10-μm testis cryo-sections from adult *CEP250*$^{+/+}$ and *CEP250*$^{-/-}$ mice (9- to 14-week-old). Scale bars: 100 μm. Dashed lines highlight the STs.
O Quantification of (N), *CEP250*$^{+/+}$ $n = 3$ mice, *CEP250*$^{-/-}$ $n = 3$ mice. 50 STs were analyzed for each mouse. See Appendix Fig S2 for ST number per section and ST diameter.

Data information: In (B, D, G, H, L, O), data are presented as mean ± SEM. n.s., not significant, $^{**}P < 0.01$, $^{****}P < 0.0001$ (the unpaired Student's *t*-test). In (B, D, G), whiskers represent the range of the data, with bottom and top represent min and max value of the dataset, respectively.

To further confirm that the testis defect associated with *CEP250* deletion was germ cell specific, the *CEP250*$^{flox/flox}$ mice were crossed with a mouse strain expressing Cre recombinase under control of the Stra8 promoter (Stra8-Cre) (Anderson *et al*, 2008). *CEP250*$^{flox/flox}$/Stra8-Cre (Stra8-*CEP250*$^{-/-}$) mice express Cre recombinase in spermatogenic cells from around P3 on (Anderson *et al*, 2008), which specifically deletes *CEP250* in germ cells. Reduction in testis size was observed in young adult Stra8-*CEP250*$^{-/-}$ mice at 8 and 15 weeks (Fig EV2A and B). MVH immunostaining revealed a reduction of germ cells at 8 weeks in Stra8-*CEP250*$^{-/-}$ testes. Germ cells were further depleted at 15 weeks, slightly later than in the whole-body Cre mice where the full depletion already happened after 9 weeks (Fig EV2C and D). This delay probably arises from the later onset of the timing of Cre recombinase expression (Anderson *et al*, 2008) as compared to whole-body CMV-Cre recombinase. Stra8-*CEP250*$^{-/-}$ mice also display fewer number and smaller size of STs at weeks 8 and 15 (Fig EV2E and F) similar to *CEP250*$^{-/-}$ mice (Appendix Fig S2). In addition, immunofluorescence staining of promyelocytic leukemia zinc finger (PLZF) protein, an undifferentiated spermatogonia marker (Costoya *et al*, 2004), and synaptonemal complex protein 1 (SCP1), a marker for differentiated spermatogonia (Di Carlo *et al*, 2000; Hoja *et al*, 2004; de Vries *et al*, 2005), showed that *CEP250*$^{flox/flox}$ mice display PLZF-positive cells at basement membrane and SCP1-positive cells in supra-basal localization seminiferous tubules (Fig EV2G, upper panel). Such organization was lost in Stra8-*CEP250*$^{-/-}$ seminiferous tubules, which contain MVH+ cells (Fig EV2G, lower panel). Overall, the phenotype observed in Stra8-*CEP250*$^{-/-}$ mice recapitulates the defects in *CEP250*$^{-/-}$ mice to confirm that *CEP250* deletion associated infertility is germ cell specific.

Loss of germ cells and defects in *CEP250* null ovary and testis is unlikely to arise from defects in germ cell lineage specification and migration

Since gonadal development is affected in both male and female *CEP250*$^{-/-}$ mice, the question arose as to whether the defects are regulated by common mechanisms during both female and male development? In mammals, male and female reproductive organs are originated from the same stem cell population, the primordial germ cells (PGCs). In mouse, PGCs come from precursor cells of the visceral ectoderm at around embryonic day E5.5. Such cells go through fate specification to become PGCs at E7.5 and subsequently migrate to colonize the gonadal ridges at around E12.5. The PGCs will subsequently go through sex determination and develop distinctively into male and female reproductive organs (Saitou & Yamaji, 2012).

We therefore examined mouse embryos at E13.5, an embryonic stage directly following the completion of PGCs migration. Both male and female *CEP250*$^{-/-}$ embryos at E13.5 were ostensibly normal and resembled *CEP250*$^{+/+}$ or *CEP250*$^{+/-}$ equivalents (Appendix Fig S3A and B). The gonadal ridges of both male and female *CEP250*$^{-/-}$ embryos also display normal appearance and size (Appendix Fig S3C–F). MVH immunostaining showed no significant difference in germ cell number of male gonadal ridges at E13.5 between *CEP250*$^{+/+}$ and *CEP250*$^{-/-}$ mice (Appendix Fig S3G and H). No significant change in germ cell number per area was observed in *CEP250*$^{-/-}$ male gonadal ridges in comparison with *CEP250*$^{+/+}$ littermates (Appendix Fig S3I). *CEP250*$^{-/-}$ female also did not seem to display difference in germ cell number as compared to the *CEP250*$^{+/-}$ (Appendix Fig S3J). Since *CEP250* null mice do not show germ cell reduction at E13.5, we conclude that PGCs lineage specification and migration are not affected by *CEP250* deletion.

Early development of male germ cells is affected by *CEP250* deletion

In a male mouse, the embryonic testis is formed after sex determination and is complete by E13.5. The GSCs undergo a period of mitotic proliferations to form spermatogonia, which can later differentiate to give rise to spermatocytes (around P5). Spermatocytes subsequently go through meiosis (around P10) and spermiogenesis (around P14) to form sperms (Fig 2A; Saitou & Yamaji, 2012). Since PGCs lineage specification and migration are unlikely to be affected

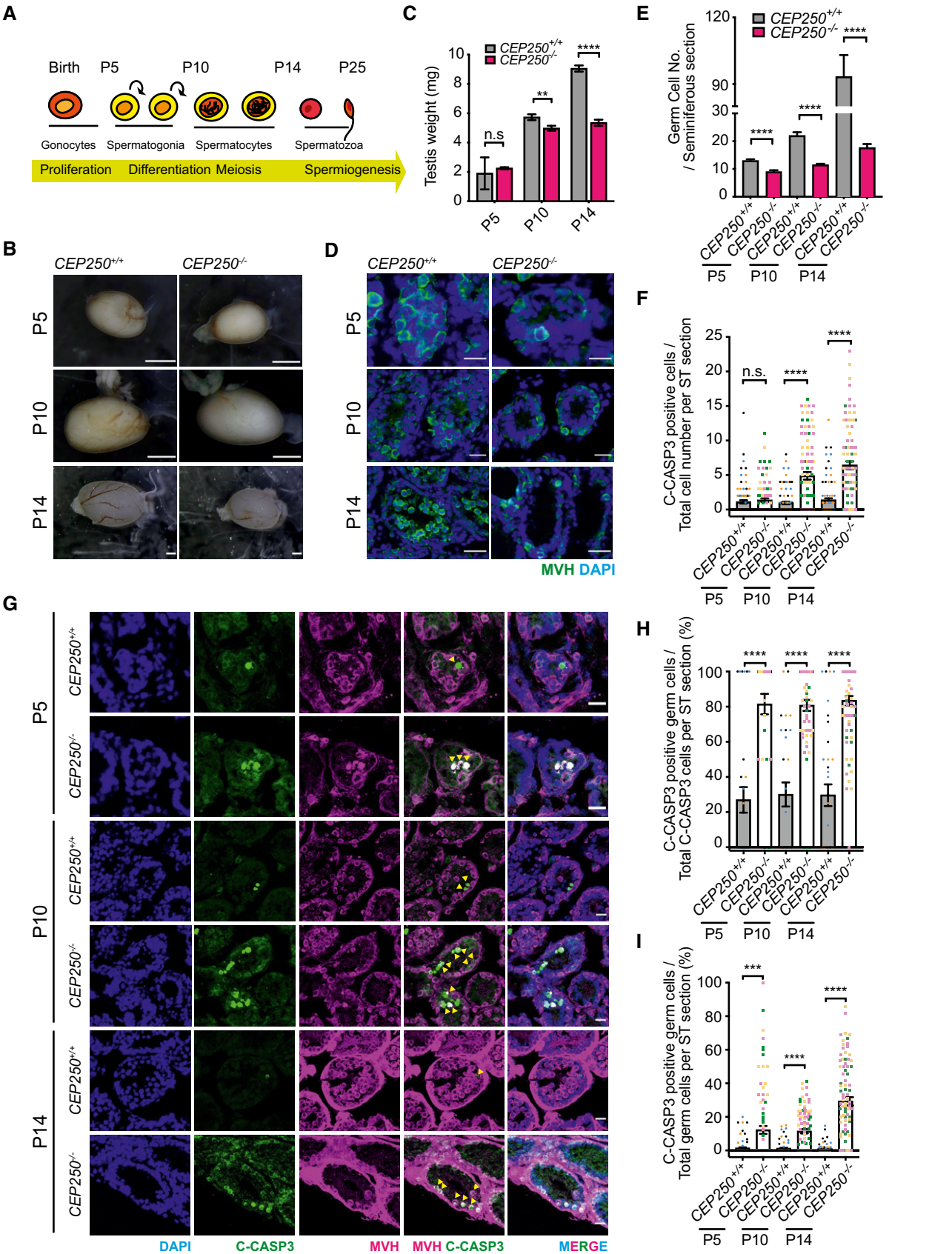
A
Birth
P5
P10
P14
P25
Gonocytes
Spermatogonia
Spermatocytes
Spermatozoa
Proliferation
Differentiation Meiosis
Spermiogenesis
B
CEP250+/+
CEP250-/-
P5
P10
P14
C
Testis weight (mg)
n.s
**
****
D
MVH DAPI
E
Germ Cell No. / Seminiferous section
F
C-CASP3 positive cells / Total cell number per ST section
n.s.
G
DAPI
C-CASP3
MVH
MVH C-CASP3
MERGE
H
C-CASP3 positive germ cells / Total C-CASP3 cells per ST section (%)
I
C-CASP3 positive germ cells / Total germ cells per ST section (%)
***

Figure 2.

Figure 2. Early development of male germ cells is affected by *CEP250* deletion, which is accompanied by increase in apoptosis.

A Illustration of spermatogenesis after birth (Saitou & Yamaji, 2012).
B Testis from neonatal mice (P5, P10 and P14). Scale bars: 500 μm.
C Quantification of testis weight from (B). P5 $CEP250^{+/+}$ $n = 5$ mice, $CEP250^{-/-}$ $n = 4$ mice, P10 $CEP250^{+/+}$ $n = 7$ mice, $CEP250^{-/-}$ $n = 4$ mice, P14 $CEP250^{+/+}$ $n = 4$ mice, $CEP250^{-/-}$ $n = 4$ mice.
D Immunofluorescence for MVH (green) with DAPI staining (blue) of 10 μm testis cryo-sections from neonatal mice (P5, P10 and P14) $CEP250^{+/+}$ and $CEP250^{-/-}$. Scale bars: 20 μm.
E Quantification of (D). $CEP250^{+/+}$ $n = 3$ mice, $CEP250^{-/-}$ $n = 3$ mice.
F Quantification of (G). C-CASP3-positive cells normalized to total cell number per seminiferous tubule (ST). Dots (colors reflect STs from different mice) represent value per ST, $CEP250^{+/+}$ $n = 3$ mice, $CEP250^{-/-}$ $n = 3$ mice. 30 STs were analyzed for each mouse.
G C-CASP3 (green) and MVH (magenta) staining with DAPI (blue) of 10-μm testis cryo-sections from neonatal mice (P5, P10, and P14) $CEP250^{+/+}$ and $CEP250^{-/-}$, scale bars: 20 μm.
H Quantification of (G). Percentage of C-CASP3 and MVH double-positive cells in relation to total C-CASP3-positive cells per ST from P5, P10, and P14 mice. Dots (colors reflect STs from different mice) represent value per ST, $CEP250^{+/+}$ $n = 3$ mice, $CEP250^{-/-}$ $n = 3$ mice. 30 STs were analyzed for each mouse.
I Quantification of (G). Percentage of C-CASP3 and MVH double-positive cells in relation to total MVH-positive cells (germ cells) per ST from P5, P10, and P14 mice. Dots (colors reflect STs from different mice) represent value per ST, $CEP250^{+/+}$ $n = 3$ mice, $CEP250^{-/-}$ $n = 3$ mice. 30 STs were analyzed for each mouse.

Data information: In (C, E), data are presented as mean ± SEM. n.s., not significant, $^{**}P < 0.01$, $^{****}P < 0.0001$ (the unpaired Student's *t*-test). In (F, H, I), data are presented as mean ± SEM. n.s., not significant, $^{***}P < 0.005$, $^{****}P < 0.0001$ (the Mann-Whitney test).

(Appendix Fig S3), we suspected that *CEP250* deletion impacts other key events during spermatogenesis. For this purpose, we examined testes from the key developmental stages P5, P10, and P14. Significant reduction in $CEP250^{-/-}$ testis weight was observed at P10 and P14 (Fig 2B and C) and MVH immunostaining showed significant reduction in germ cell numbers from P5 onward with a further decrease at P10 and P14 (Fig 2D and E). In addition, elimination of *CEP250* promoted apoptosis of GSCs as indicated by an increase in cleaved Caspase-3 (C-CASP3)-positive cells in neonatal testis (P10 and P14) (Fig 2F and G). By contrast, no significant difference was detected in the number of total C-CASP3-positive cells between $CEP250^{+/+}$ and $CEP250^{-/-}$ testis at P5 (Fig 2F and G). However, co-examination of MVH immunostaining revealed that over 80% of C-CASP3 positive cells in $CEP250^{-/-}$ testis were also immunostained with the germ cell marker MVH at all developmental stages examined (P5, P10, and P14). In stark contrast, merely a small proportion, approximately 30% of C-CASP3-positive cells in $CEP250^{+/+}$ testis, was marked with MVH marker (Fig 2G and H). This indicates that apoptotic population in $CEP250^{-/-}$ testis was majorly composed of germ cells, differing from that of $CEP250^{+/+}$ where only a small proportion of apoptotic cells appeared to be germ cells (Fig 2H). As a result, significant higher percentage of apoptotic germ cells in relation to total germ cell was detected in in $CEP250^{-/-}$ testis at P5, P10, and P14 (Fig 2G and I). In summary, $CEP250^{-/-}$ mice show defects in early testis development, which may attribute to perturbation to early developmental events of male germ cells.

Loss of *CEP250* leads to premature differentiation of spermatogonia

The PLZF protein is used as a marker of GSC because it is expressed in undifferentiated spermatogonia and is required for the GSC function (Lovelace *et al*, 2016). Examination of $PLZF^+$ cells revealed an evident reduction in the number of undifferentiated spermatogonia in $CEP250^{-/-}$ mice from P5 onward (Fig 3A and B), indicative of a premature loss of GSC.

To analyze this GSC depletion further, we monitored the fate of PLZF expressing undifferentiated (PLZF positive) and SCP1 expressing differentiated (SCP1 positive) spermatogonia during development. Interestingly, PLZF and SCP1 double staining showed an intermediate population of spermatogonia, corresponding to differentiating spermatogonia, which expressed both PLZF and SCP1 (Fig 3C and D). We observed a significant increase of differentiated $PLZF^-$ $SCP1^+$ spermatogonia in $CEP250^{-/-}$ mice already at P2 at the expense of the loss of $PLZF^+$ SCP1+ and $PLZF^+$ $SCP1^-$ populations (Fig 3C and E, arrow heads in C indicate the presence of green

Figure 3. Loss of *CEP250* leads to premature differentiation.

A Immunofluorescence staining for PLZF (red) with DAPI staining (blue) of 10 μm cryo-sections of testes from $CEP250^{+/+}$ and $CEP250^{-/-}$ mice at P5, P10, and P14. Scale bars: 20 μm.
B Quantification of (A). Quantification of PLZF+ cells per seminiferous (ST) section of $CEP250^{+/+}$ and $CEP250^{-/-}$, testes at P5, P10, and P14. Dots (colors reflect STs from different mice) represent value per ST, $CEP250^{+/+}$ (P5) $n = 3$ mice, $CEP250^{-/-}$ (P5) $n = 3$ mice, 50 STs were analyzed for each mouse; $CEP250^{+/+}$ (P10) $n = 3$ mice, $CEP250^{-/-}$ (P10) $n = 3$ mice, at least 30 STs were analyzed for each mouse; $CEP250^{+/+}$ (P14) $n = 3$ mice, $CEP250^{-/-}$ (P14) $n = 3$ mice, at least 50 ST were analyzed for each mouse.
C Immunofluorescence staining for SCP1 (green), PLZF (red), and DAPI (blue) of 10 μm cryo-sections of testes from $CEP250^{+/+}$ and $CEP250^{-/-}$ mice at P2, P3, P5, and P7. Arrowheads highlight PLZF- SCP1+ (green) cells, which represent differentiated spermatogonia. Scale bars: 20 μm.
D Illustration of sequential spermatogonia differentiation and formation of seminiferous tubules.
E–H Quantification of (C). The number of PLZF+ SCP1-, PLZF+ SCP1+, PLZF-, and SCP1+ cells normalized to total cell number per ST section in $CEP250^{+/+}$ and $CEP250^{-/-}$ testes at P2, P3, P5, and P7, respectively. Dots (colors reflect STs from different mice) represent value per ST, $CEP250^{+/+}$ (P2-P7) $n = 3$ mice, $CEP250^{-/-}$ (P2-P7) $n = 3$ mice, at least 40 STs were analyzed for each mouse.
I Summary of proportion of PLZF+ SCP1-, PLZF+ SCP1+, PLZF-, and SCP1- cells per ST section in $CEP250^{+/+}$ and $CEP250^{-/-}$ testes from P2-P7.

Data information: In (B, E–H), data are presented as mean ± SEM. n.s., not significant, $^{*}P < 0.05$, $^{***}P < 0.005$, $^{****}P < 0.0001$ (the Mann–Whitney test).

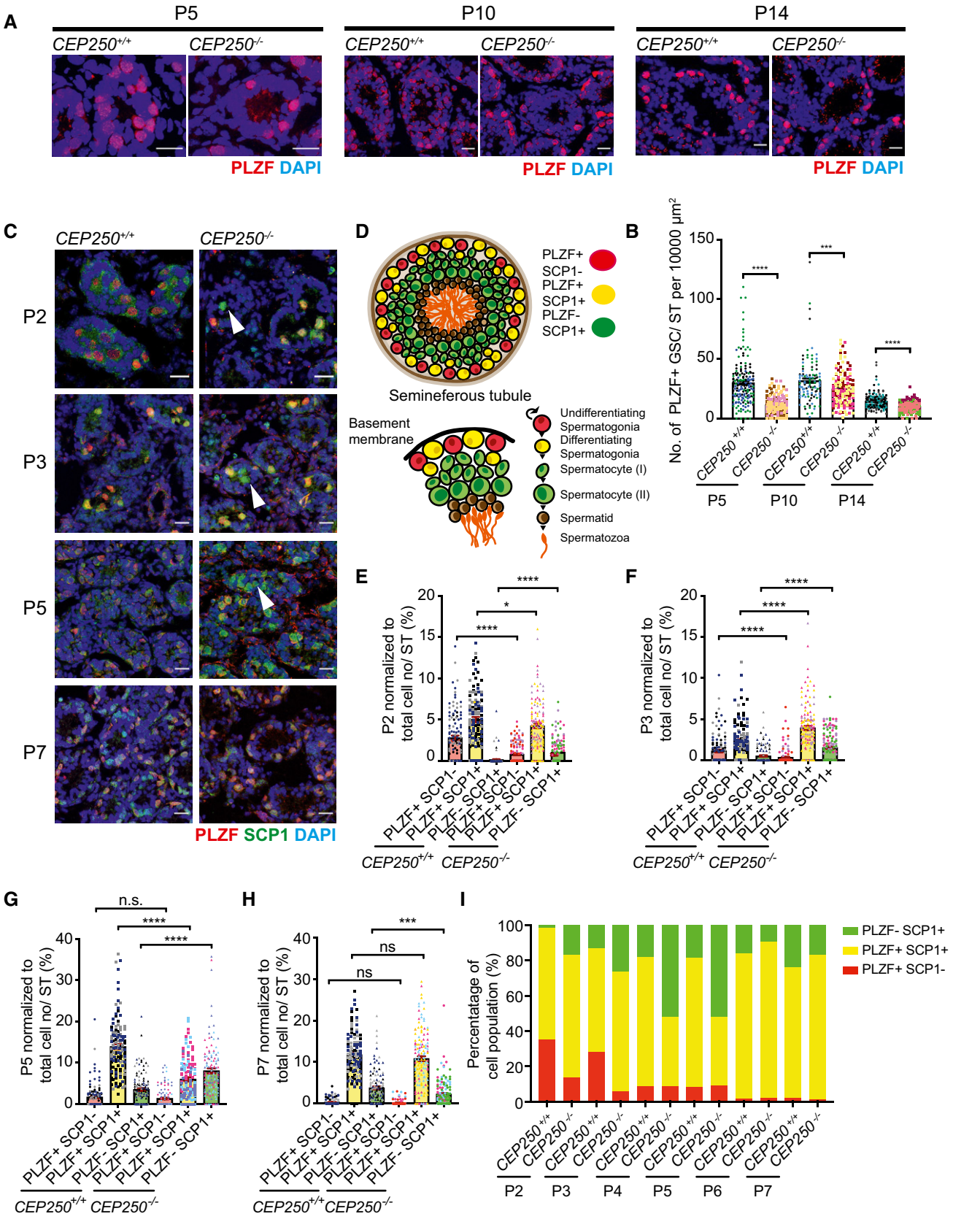
A
P5
P10
P14
CEP250+/+
CEP250-/-
PLZF DAPI
C
P2
P3
P5
P7
PLZF SCP1 DAPI
D
PLZF+ SCP1-
PLZF+ SCP1+
PLZF- SCP1+
Semineferous tubule
Basement membrane
Undifferentiating Spermatogonia
Differentiating Spermatogonia
Spermatocyte (I)
Spermatocyte (II)
Spermatid
Spermatozoa
B
No. of PLZF+ GSC/ ST per 10000 μm2
E
P2 normalized to total cell no/ ST (%)
F
P3 normalized to total cell no/ ST (%)
G
P5 normalized to total cell no/ ST (%)
H
P7 normalized to total cell no/ ST (%)
n.s.
ns
I
Percentage of cell population (%)
PLZF- SCP1+
PLZF+ SCP1+
PLZF+ SCP1-

Figure 3.

PLZF$^-$ SCP1$^+$ cells). Such changes persisted until P5 (Fig 3C, F and G; summarized in Fig 3I). At P7, a reduction of PLZF$^-$ SCP1$^+$ spermatogonia was observed in *CEP250*$^{-/-}$ mice in comparison to that of *CEP250*$^{+/+}$, indicating a defect in maintenance of the prematurely differentiated PLZF$^-$ SCP1$^+$ spermatogonia (Fig 3C and H) driven by increased apoptosis (Fig 2F–H). To rule out the possibility that the reduction of undifferentiated spermatogonia (PLZF$^+$ SCP1$^-$ population) in *CEP250*$^{-/-}$ mice could also be a result of germ cell depletion from earlier developmental stages, we examined the total germ cell numbers before the onset of premature differentiation (P2) by MVH immunostaining. *CEP250*$^{+/+}$ and *CEP250*$^{-/-}$ mice showed comparable germ cell numbers at P1 (Appendix Fig S4A–C). Taken together, these observations reveal a premature differentiation of spermatogonia in *CEP250*$^{-/-}$ mice, which might contribute to premature loss of GSCs.

CEP250$^{-/-}$ mice show premature apical translocation of GSCs into the seminiferous tubule lumen

Germ stem cells reside close to the basement membrane of seminiferous tubules (de Rooij, 2017). When spermatogonia differentiate, they translocate apically into the lumen of the seminiferous tubule, where they will later undergo a succession of differentiation events into spermatocytes (Fig 4A). We found that in *CEP250*$^{+/+}$ mice, PLZF$^-$ SCP1$^+$ and PLZF$^+$ SCP1$^+$ spermatogonia cannot be detected inside the lumen of seminiferous tubule until P6 (Fig 4B, white arrow heads). In stark contrast, quantification of the location of differentiated spermatogonia revealed an increase of centrally located total SCP1$^+$ spermatogonia (PLZF$^+$ SCP1$^+$ and PLZF$^-$ SCP1$^+$) in *CEP250*$^{-/-}$ mice from P4 onward (Fig 4B–G). Notably, centrally located PLZF$^-$ SCP1$^+$ spermatogonia decreased at P7 in *CEP250*$^{-/-}$ mice (Fig 4B and G), indicating possible defects in the maintenance of the differentiated spermatogonia when the centrosome linker function is abolished. This is consistent with the observation made earlier by the reduction of PLZF$^-$ SCP1$^+$ spermatogonia number in *CEP250*$^{-/-}$ mice at P7 (Fig 3C and H) and the elevation of apoptotic germ cells (Fig 2F–I). In conclusion, *CEP250*$^{-/-}$ mice show premature differentiation of spermatogonia development alongside premature translocation of the differentiated spermatogonia into the seminiferous tubule lumen. The prematurely differentiated and translocated spermatogonia show defects in GSC maintenance and possibly undergo apoptosis later, which eventually results in the total loss of the germ cells.

CEP250$^{-/-}$ mice show defects in meiotic progression

Our findings indicate that *CEP250*$^{-/-}$ testis displays steady increase of apoptotic cells between P10 and P14 (Fig 2F–I), during which time the spermatocytes are expected to undergo the first round of meiotic divisions (Griswold, 2016). We thereupon examined the fate of the meiotic spermatocytes at P10 and P13. We immunostained the testis sections, using SCP1 to mark the spermatocytes and γH2AX to mark the double-strand breaks (DSBs) formed during meiosis I (Turner *et al*, 2004). We characterized the substages of meiotic prophase I in spermatocytes based on distinct γH2AX patterns (Mahadevaiah *et al*, 2001; Bolcun-Filas *et al*, 2007). We found that at P10 *CEP250*$^{+/+}$ testis displayed spermatocytes at leptotene stage, a stage which is characterized by spread-out localization of SCP1 across the nucleus and increase of number and intensity of γH2AX foci, indicating the initiation of meiosis I (Appendix Fig S5A). Nevertheless, although leptotene spermatocytes were also found in the *CEP250*$^{-/-}$ testis, a noticeable proportion of *CEP250*$^{-/-}$ spermatocytes showed dysregulated γH2AX pattern as indicated by the only partial staining of γH2AX-positive domains (Appendix Fig S5A). At P13, *CEP250*$^{+/+}$ spermatocytes displayed 3 consecutive substages of meiosis I, i.e., leptotene, zygotene and pachytene stages. Zygotene stage is marked with filamentous SCP1 elements as well as decrease of number whilst increase in concentration of γH2AX-positive domains along the stretched SCP1 elements. γH2AX-positive domains subsequently dissolve from the autosomal chromatins and appear only on the sex chromatin as one concentrated dot-like structure (Mahadevaiah *et al*, 2001; Turner *et al*, 2004). In contrast, *CEP250*$^{-/-}$ spermatocytes displayed only an aberrant pattern in which SCP1 signal was diffusely located across the nucleus and γH2AX signal did not concentrate on a defined localization as this was the case in pachytene of the *CEP250*$^{+/+}$ wildtype. Our finding suggests that *CEP250*$^{-/-}$ spermatocytes are able to initiate meiosis, nonetheless meiosis I cannot be completed, which may contribute extensive apoptosis in germ cells (Fig 2F–I) and reduction of germ cells (Fig 2D and E) from P10 onwards.

Figure 4. *CEP250*$^{-/-}$ mice show premature apical translocation of GSCs into the seminiferous tubule lumen.

A Schematic diagram showing translocation of differentiating spermatogonia.

B Representative images of mouse seminiferous tubule (ST) sections stained for PLZF (red), SCP1 (green), and DAPI (blue) at P4, P6, and P7. Scale bars: 20 μm. Arrowheads highlight PLZF$^-$ SCP1$^+$ (green) cells localize to the middle of the ST lumen, which represent differentiated spermatogonia that translocated to the middle of the ST lumen.

C Quantification of (B). Shown is the number of PLZF$^-$ SCP1$^+$ cells, which translocated inwards the seminiferous tubule lumen per seminiferous tubule section, as normalized to the total cell number per ST section. Dots (colors reflect STs from different mice) represent value per ST, *CEP250*$^{+/+}$ (P4-P7) $n = 3$ mice, *CEP250*$^{-/-}$ (P4-P7) $n = 3$ mice, at least 30 STs were analyzed for each mouse.

D Quantification of (B). Shown is the total number of SCP1$^+$ cells, which translocated inwards the seminiferous tubule lumen per ST section, as normalized to the total cell number per seminiferous tubule section. Dots (colors reflect STs from different mice) represent value per ST, *CEP250*$^{+/+}$ (P4-P7) $n = 3$ mice, *CEP250*$^{-/-}$ (P4-P7) $n = 3$ mice, at least 30 STs were analyzed for each mouse.

E Quantification of (B). Shown is the number of PLZF$^+$ SCP1$^+$ cells which translocated inwards the seminiferous tubule lumen per seminiferous tubule section, as normalized to the total cell number per seminiferous tubule section. Dots (colors reflect STs from different mice) represent value per ST, *CEP250*$^{+/+}$ (P4-P7) $n = 3$ mice, *CEP250*$^{-/-}$ (P4-P7) $n = 3$ mice, at least 30 STs were analyzed for each mouse.

F Summary of proportion of PLZF$^+$ SCP1$^+$ cells, which translocated inside the seminiferous tubule per section against which remained at the basal membrane.

G Summary of proportion of PLZF$^-$ SCP1$^+$ cells, which translocated inside the seminiferous tubule per section againt which remained at the basal membrane.

Data information: In (C–E), data are presented as mean ± SEM. n.s., not significant, *$P < 0.05$, **$P < 0.01$, ***$P < 0.005$ (the Mann–Whitney test).

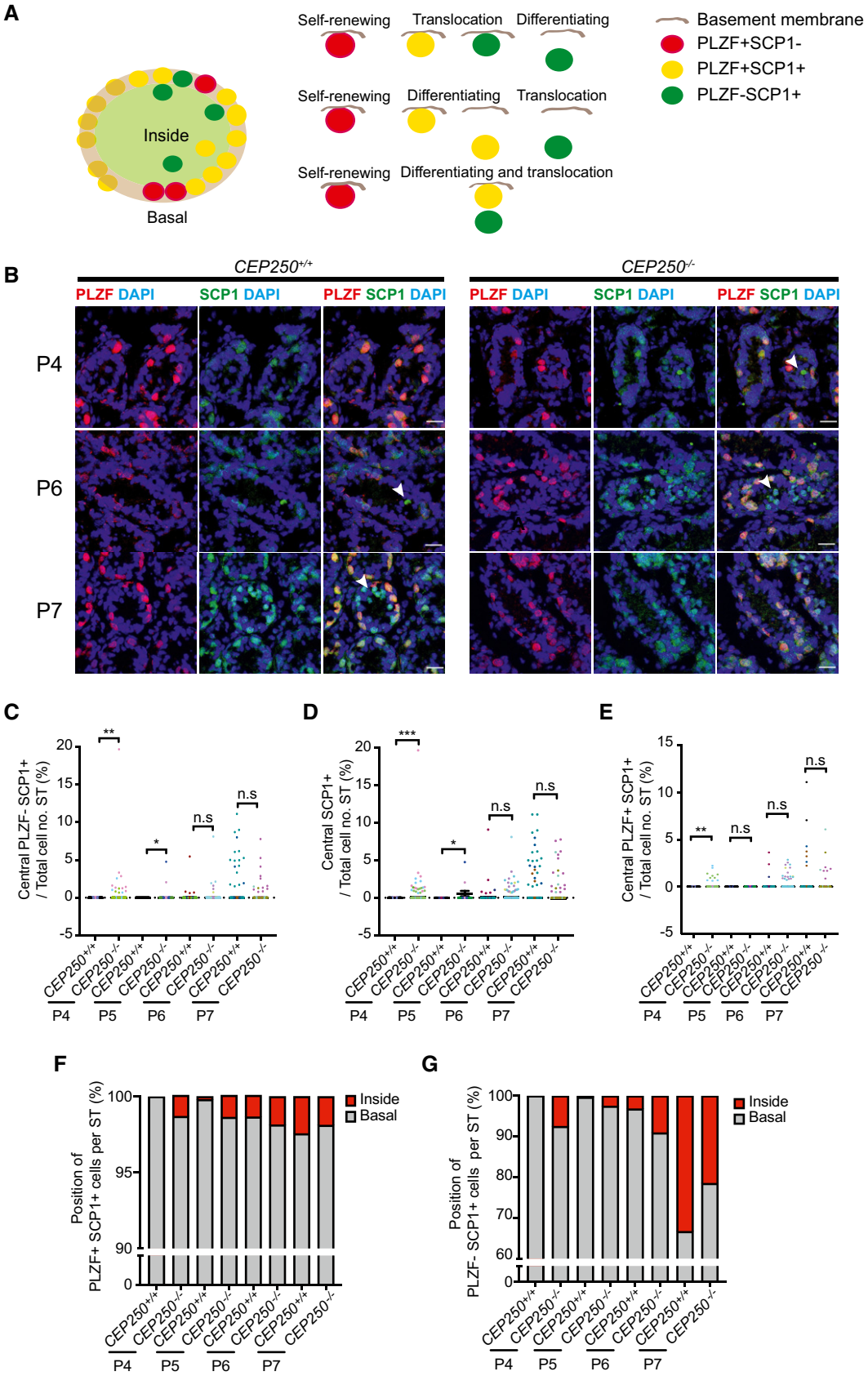
A
Inside
Basal
Self-renewing
Translocation
Differentiating
Self-renewing
Differentiating
Translocation
Self-renewing
Differentiating and translocation
Basement membrane
PLZF+SCP1-
PLZF+SCP1+
PLZF-SCP1+
B
CEP250+/+
CEP250-/-
PLZF DAPI
SCP1 DAPI
PLZF SCP1 DAPI
P4
P6
P7
C
Central PLZF- SCP1+ / Total cell no. ST (%)
D
Central SCP1+ / Total cell no. ST (%)
E
Central PLZF+ SCP1+ / Total cell no. ST (%)
n.s
P4
P5
P6
P7
F
Position of PLZF+ SCP1+ cells per ST (%)
Inside
Basal
G
Position of PLZF- SCP1+ cells per ST (%)

Figure 4.

CEP250 regulates the oriented division of male GCs

During GSC division, mitotic spermatogonia choose to orient the spindle either parallel or perpendicular to the basement membrane (Lagos-Cabré & Moreno, 2008; Neumüller & Knoblich, 2009). Self-expansion by vertical stem cell division produces two daughter stem cells, whereas perpendicular stem cell division yields one differentiating daughter cell and one retaining the fate of being a stem cell (Neumüller & Knoblich, 2009). To determine whether the loss of centrosome cohesion had an impact upon this precision control of spindle orientation we assessed spindle angle in sections of P4 and P5 seminiferous tubules of $PLZF^+$ GSCs (Fig 5A and B, Appendix Fig S6A and B). Mitotic cells were marked with phospho-histone H3 (PH3) and the centrosomes with γ-tubulin antibodies. The orientation of the mitotic spindle was determined by drawing a straight white line between the two centrosomes (Appendix Fig S6A and B). At P4, 76% of dividing $CEP250^{+/+}$ GSCs displayed a metaphase spindle at an orientation of within 10° of being parallel to the basement membrane (dashed yellow line), indicating substantial expansion divisions in the $CEP250^{+/+}$ GSCs at this stage of development. By contrast, only 17% of mitotic GSCs in $CEP250^{-/-}$ mice show parallel spindles (Appendix Fig S6A, C and E). At P5, two major populations of dividing GSCs were observed in $CEP250^{+/+}$ mice: the one with a mitotic spindle perpendicular, close to 90° to the basement membrane (27%) and those with a mitotic spindle parallel to the basement membrane (43%) (Appendix Fig S6B, D and F). This was different in mitotic cells from $CEP250^{-/-}$ mice that displayed a randomized mitotic spindle orientation with only 17% of mitotic GSCs showing a parallel spindle orientation (0–10°) (Appendix Fig S6B, D and F). Though a number of studies have determined spindle orientation in metaphase in mouse tissues (Dumont *et al*, 2015; Gai *et al*, 2016; Li *et al*, 2016; Vargas-Hurtado *et al*, 2019) as well as in other model organisms (Hehnly *et al*, 2015), we were concerned that spindle orientation might change from metaphase to anaphase due to dynamic behavior (Kiyomitsu & Cheeseman, 2013). Hence, we further validated our finding focusing exclusively on anaphase spindles in spermatogonia at P4 and P5. Indeed, similar patterns of spindle angle as in metaphase cells (Appendix Fig S6) were observed between $CEP250^{+/+}$ and $CEP250^{-/-}$ mice at P4 and P5 (Fig 5A–F). This suggests that the spindle does not flip from metaphase to anaphase in GSC divisions on P4 and P5.

These findings indicate that deletion of *CEP250*, hence disruption of centrosome cohesion, may have an adverse impact on the development of GSCs within seminiferous tubules by compromising the ordered orientation of the division plane. Thus, there appear to be two outcomes arising from the loss of *CEP250* function in GSCs. The existing stem cell population divides obliquely, which may result in premature differentiation, thereby diminishing the total stem cell population (Fig 5G). As result, GSCs leave the basement membrane and translocate into the ST lumen prematurely (Fig 4). The spatial and temporal mis-regulation of the $CEP250^{-/-}$ GSCs will lead to an increase in germ cell apoptosis (Fig 2F–I).

$CEP250^{-/-}$ mice show defects in E-cadherin-related cell polarity change during cell cycle progression

Cell polarity control of the expansion and differentiation of stem cells has been shown to underpin the correct architecture and function of a number of tissues in a variety of organisms (Martin-Belmonte & Perez-Moreno, 2012). Among a rank of cell polarity proteins studied, the role of E-cadherin in *Drosophila* germ stem cell development is well characterized (Jenkins *et al*, 2003; Tsukita *et al*, 2009). E-cadherin is also a surface marker for germ stem cells in mice (Tolkunova *et al*, 2009). Therefore, sections of P5 seminiferous tubules were examined by immunofluorescence to assess E-cadherin expression. Consistent with previous findings (Tolkunova *et al*, 2009), our study found that in young mouse testes, E-cadherin was exclusively expressed in $PLZF^+$ GSCs, the undifferentiated spermatogonia, indicating it may serve as a germ stem cell surface marker (Fig 6A, B, D and F).

Next, we determined how E-cadherin distribution in P5 GSC changed as cells transited the cell division cycle by using PH3 as mitotic marker. We observed notably different patterns of E-cadherin enrichment on the GSC surface, of which two patterns are particularly pronounced. In a non-polarized category, E-cadherin was detected across the entire cell surface. In the basal-polarized group, E-cadherin was found in the region, which was in contact or close to the basement membrane. Apical polarized and side polarized cells were also seen alongside a population where E-cadherin was not expressed, referred to as null (Fig 6A).

During interphase the majority of GSCs (close to 75%) display a non-polarized E-cadherin pattern for both $CEP250^{+/+}$ and $CEP250^{-/-}$ mice. Notably, a subpopulation of GSCs (close to 15%) display basal-polarized E-cadherin pattern, which applies to both $CEP250^{+/+}$ and $CEP250^{-/-}$ mice (Fig 6B and C). Additional minor phenotypes were

Figure 5. *CEP250* regulates the oriented division of male GCs.

A Representative images of P4 mouse seminiferous tubule (ST) 10 μm cryo-sections stained for PLZF (red), γ-Tubulin (green), PH3 (magenta), and DAPI (blue). Arrowheads highlight the centrosomes. Dashed yellow line highlights the basement membrane. Semi-transparent white line, which bisects both spindle poles, was used to determine spindle angle Ø orientation in relation to the basement membrane. Anaphase cells were analyzed. Scale bars: 5 μm.

B Representative images of P5 mouse seminiferous tubule 10 μm cryo-sections stained for PLZF (red), γ-Tubulin (green), PH3 (magenta), and DAPI (blue). Arrowheads highlight the centrosomes. Dashed yellow line highlights the basement membrane. Semi-transparent white line, which bisects both spindle poles, was used to determine spindle angle Ø orientation in relation to the basement membrane. Anaphase cells were analyzed. Scale bars: 5 μm.

C–F (C, E) Quantitation of spindle angle of anaphase GSCs in P4 ST sections (from A). Spindle angle relative to basement membrane for $CEP250^{+/+}$ and $CEP250^{-/-}$. In (C), dots (colors reflect different mice) represent spindle angle of each GSC. In (E), the three dots represent averaged spindle angle per mouse. $CEP250^{+/+}$ $n = 3$ mice, $CEP250^{-/-}$ $n = 3$ mice. At least 10 cells were analyzed for each mouse. (D, F) Quantitation of spindle angle of anaphase GSCs in P5 ST sections (from B). As (C, E) but for P5. In (D), dots (colors reflect different mice) represent spindle angle of each GSC. In (F), the three dots represent averaged spindle angle per mouse. $CEP250^{+/+}$ $n = 3$ mice, $CEP250^{-/-}$ $n = 3$ mice. At least 10 cells were analyzed in each mouse.

G Schematic diagram showing spindle angles relative to basement membrane were identified for $CEP250^{+/+}$ and $CEP250^{-/-}$ GSCs. The spindle angle of $CEP250^{+/+}$ mitotic GSCs mainly fall into two distinct populations. First, between 0° and 10°, indicating self-expansion. Second, between 75° and 90°, indicating differentiation. By contrast, $CEP250^{-/-}$ mitotic GSCs display more randomized distribution of spindle angles.

Data information: In (E, F), data are presented as mean ± SEM. n.s., not significant, $*P < 0.05$, $***P < 0.005$ (the unpaired Student's *t*-test).

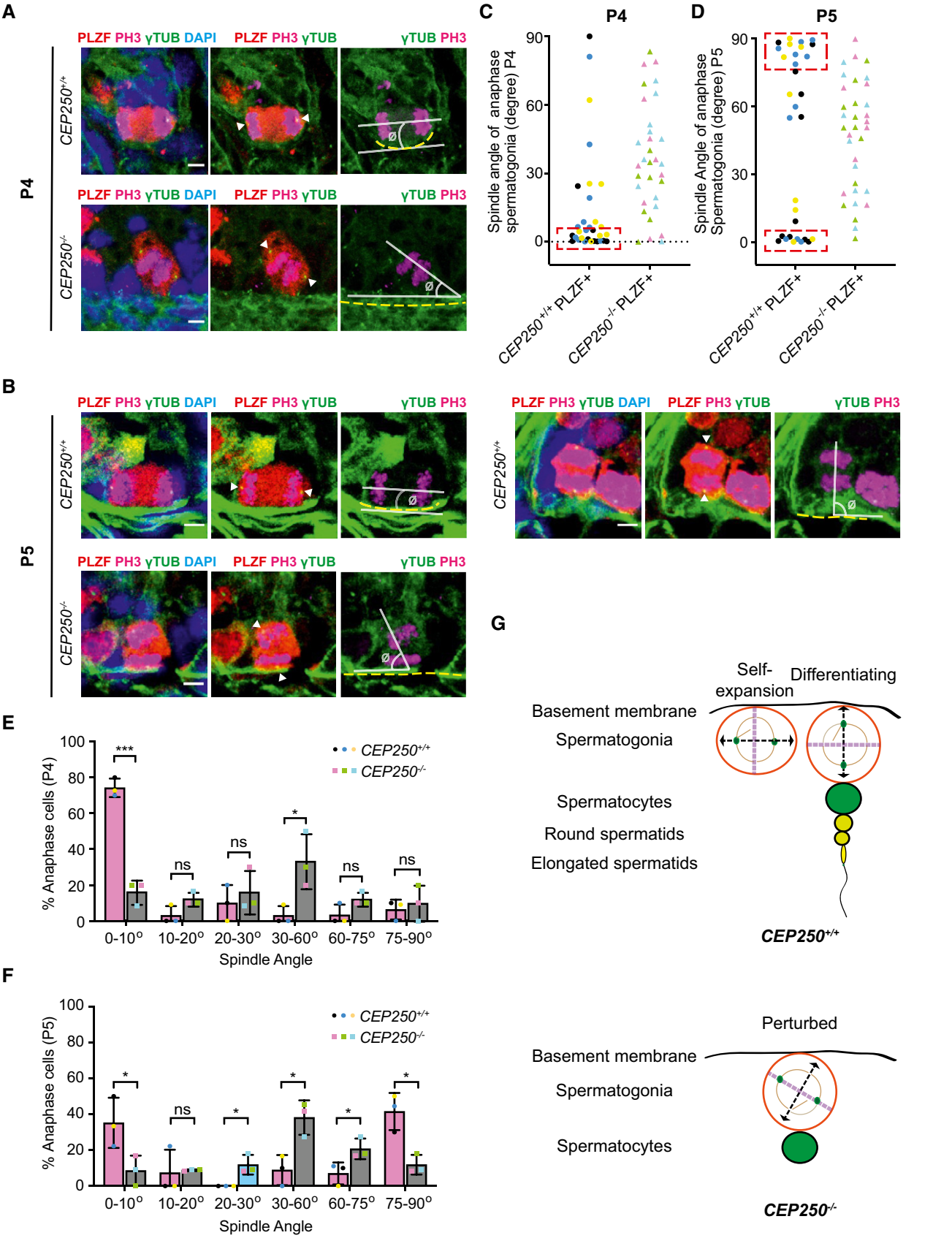
A
P4
PLZF PH3 γTUB DAPI
PLZF PH3 γTUB
γTUB PH3
CEP250+/+
CEP250-/-
B
P5
C
P4
Spindle angle of anaphase spermatogonia (degree) P4
CEP250+/+ PLZF+
CEP250-/- PLZF+
D
P5
Spindle Angle of anaphase Spermatogonia (degree) P5
E
% Anaphase cells (P4)
Spindle Angle
0-10°
10-20°
20-30°
30-60°
60-75°
75-90°
***
ns
*
F
% Anaphase cells (P5)
G
Self-expansion
Differentiating
Basement membrane
Spermatogonia
Spermatocytes
Round spermatids
Elongated spermatids
CEP250+/+
Perturbed
CEP250-/-

Figure 5.

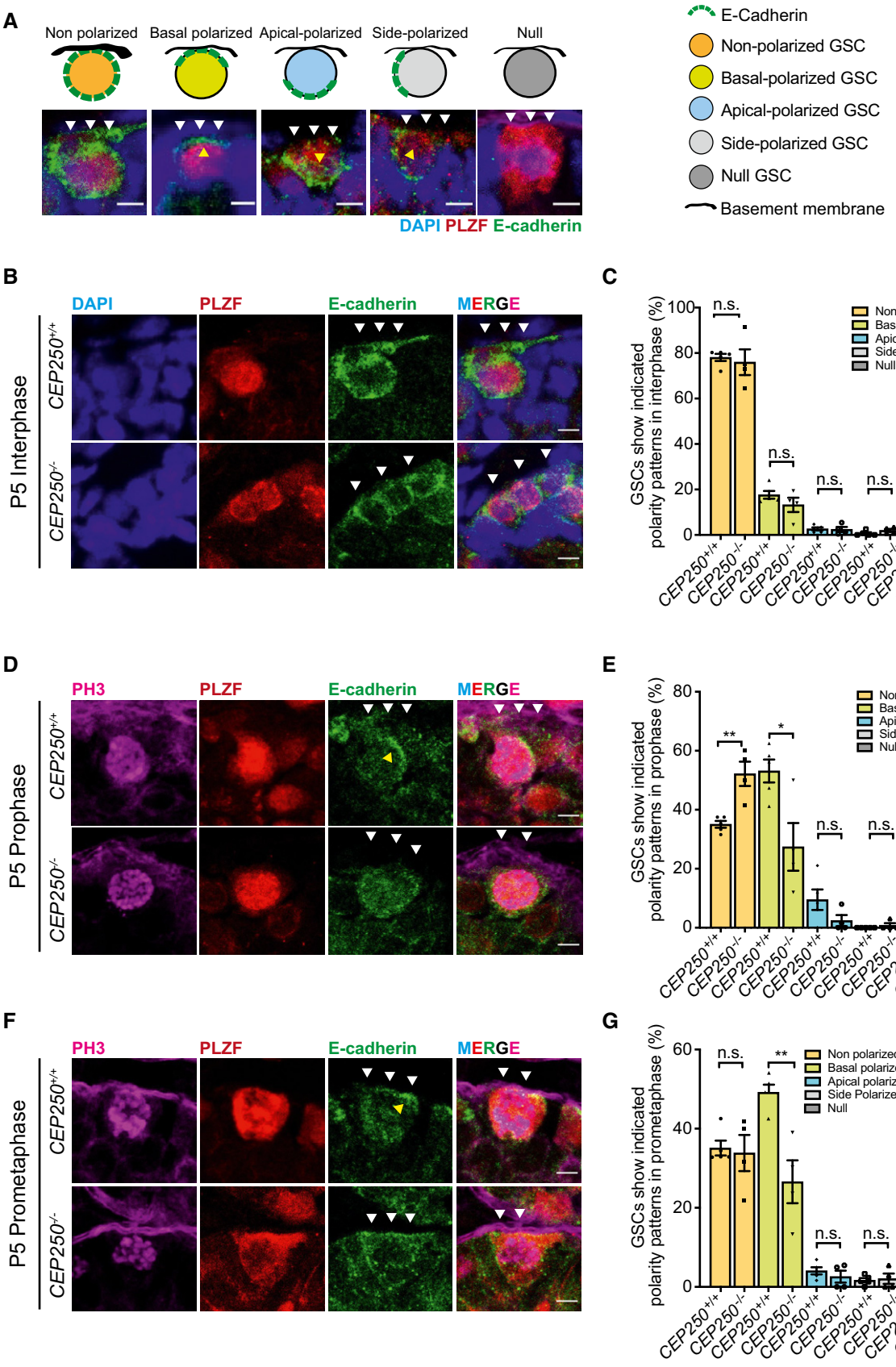

Figure 6.

Figure 6. *CEP250*$^{-/-}$ mice show defects in E-cadherin polarity change during cell cycle progression.

A Illustration showing distinctive polarity patterns regarding E-cadherin in GSCs. The patterns were classified using following criteria. "Non-polarized: nearly continuous signal of E-cadherin patches across the cell cortex; basal-polarized: preferable localization of E-cadherin to the side of cell cortex close to the basement membrane; apical polarized: preferable localization of E-cadherin to the side of cell cortex pointing away from the basement membrane; side polarized: preferable localization of E-cadherin to the side of cell cortex, which is nearly perpendicular to the basement membrane; null: no E-cadherin signal on the cell cortex." The representative immunofluorescence images for each pattern were shown below the illustrations. 10 μm cryo-sections stained for PLZF (red), E-cadherin (green), and DAPI (blue) showing non-polarized, basal-polarized, apical polarized pattern, respectively. Note, the non-polarized cell example in (A) is identical to the *CEP250*$^{+/+}$ cell shown in (B). The basal-polarized cell example in (A) is identical to the *CEP250*$^{+/+}$ cell shown in Fig EV3C.

B Representative images of P5 mouse ST. 10-μm cryo-sections stained for PLZF (red), E-cadherin (green), and DAPI (blue) showing GSCs in interphase. Scale bars: 5 μm.

C Quantification of (B). Percentage of GSCs displaying different polarity status are indicated. *CEP250*$^{+/+}$ $n = 5$ mice, *CEP250*$^{-/-}$ $n = 4$ mice. At least 100 cells were analyzed in each mouse and the average was calculated for each mouse.

D Representative images of P5 mouse ST. 10 μm cryo-sections stained for PLZF (red), E-cadherin (green) and PH3 (magenta) showing GSCs in prophase. PH3 staining marks the mitotic chromatin. Scale bars: 5 μm.

E Quantification of (D). Percentage of GSCs displaying different polarity status are indicated. *CEP250*$^{+/+}$ $n = 5$ mice, *CEP250*$^{-/-}$ $n = 4$ mice. At least 10 cells were analyzed in each mouse and the average was calculated for each mouse.

F Representative images of P5 mouse ST 10 μm cryo-sections stained for PLZF (red), E-cadherin (green) and PH3 (magenta) showing GSCs in prometaphase. PH3 staining marks the mitotic chromosome condensation. Scale bars: 5 μm.

G Quantification of (F), percentage of GSCs displaying different polarity status are indicated. *CEP250*$^{+/+}$ $n = 5$ mice, *CEP250*$^{-/-}$ $n = 4$ mice. At least 30 cells were analyzed in each mouse, and the average was calculated for each mouse.

Data information: In A, B, D, and F, white arrowheads highlight basement membrane; yellow arrowhead highlights cortical enrichment of E-cadherin toward the basement membrane. In (C, E, G), data are presented as mean ± SEM. n.s., not significant, *$P < 0.05$, **$P < 0.01$, ***$P < 0.005$ (the unpaired Student's *t*-test).

equally observed in *CEP250*$^{+/+}$ and *CEP250*$^{-/-}$ GSCs (Fig 6C). In conclusion, in interphase the polarity patterns of E-cadherin in GSCs do not differ between *CEP250*$^{+/+}$ and *CEP250*$^{-/-}$ mice (Fig 6B and C).

Importantly, a sharp increase in the polarized E-cadherin population was observed in *CEP250*$^{+/+}$ GSCs during prophase and prometaphase (Fig 6D–G, indicated by yellow arrowheads). By contrast, the increase of basal-polarized E-cadherin GSC population in *CEP250*$^{-/-}$ mice was significantly reduced compared to *CEP250*$^{+/+}$ mice. As a result, only 29% (prophase) and 35% (prometaphase) of *CEP250*$^{-/-}$ GSCs showed a basal-polarized E-cadherin pattern, which was clearly less than the 53% (prophase) and 50% (prometaphase) of the population observed in *CEP250*$^{+/+}$ GSCs (Fig 6D–G). Meanwhile, a significantly larger proportion of GSCs showed non-polarized E-cadherin pattern in *CEP250*$^{-/-}$ mice when compared to their *CEP250*$^{+/+}$ counterparts during prophase (Fig 6E). This decline in basal-polarized GSCs was accompanied by an increase in the frequency of null cells throughout mitosis (Fig 6C, E and G). Other E-cadherin polarity patterns were also seen in a small proportion of prophase GSCs.

In order to investigate whether the E-cadherin polarity pattern switch was merely involved in mitotic GSCs during differentiation (P5), we additionally checked it in GSCs of P2 *CEP250*$^{+/+}$ and *CEP250*$^{-/-}$ mice during mitosis, a stage when most of the GSCs undergo stem cell self-expansion. Importantly, similar E-cadherin patterns were found in P2 *CEP250*$^{+/+}$ GSCs as seen in P5, with *CEP250*$^{-/-}$ GSCs displaying defects in the polarity switch (Fig EV3A–F). Such observation suggests that the specific changes of E-cadherin polarity patterns in mitotic GSCs are not exclusive to differentiating GSCs but influence both proliferating and differentiating GSCs.

Figure 7. *CEP250* regulates centrosome cohesion and centrosome positioning in GSCs during mitosis.

A Representative images of P5 mouse seminiferous tubule (ST) 10 μm cryo-sections stained for PLZF (red), ODF2 (green), NIN (magenta), and PH3 (blue) showing GSCs in prophase. Scale bars: 2 μm. Yellow arrowheads highlight the two centrosomes.

B Quantification of (A). Centrosome distance in GSCs in prophase at P5. *CEP250*$^{+/+}$ $n = 3$ mice, *CEP250*$^{-/-}$ $n = 3$ mice. At least 50 cells were analyzed in each mouse (color of dot indicates mouse). Dashed line indicates 4 μm as the threshold of well separated centrosomes.

C Illustration showing methodology to determine the mother centrosome and the daughter centrosome. In brief, the intensity of centrosomal NIN and ODF2 in GSCs in prometaphase was measured. The ratio of centrosomal NIN or ODF2 intensities of centrosomes close vs. far from the basement membrane in one GSC was calculated. Thresholds were drawn at 85 and 115%, indicating > 15% difference. A GSC with both NIN and ODF2 intensity ratio < 85% was considered to display mother centrosome close to the basement membrane. A GSC with both NIN and ODF2 intensity ratio > 115% was considered to display daughter centrosome close to the basement membrane.

D Representative images of P5 mouse seminiferous tubule 10-μm cryo-sections stained for PLZF (red), ODF2 (green), NIN (magenta), and PH3 (blue), focusing on PLZF+ germ stem cells (GSCs) in prometaphase. Scale bars: 2 μm. Yellow lines highlight basement membrane. Yellow arrowheads highlight the mother centrosomes and white arrowheads highlight the daughter centrosomes.

E Quantification of (D). Percentage of prometaphase GSCs, which preferentially position their mother centrosome close to the basement membrane in *CEP250*$^{+/+}$ and *CEP250*$^{-/-}$ testis at P5. *CEP250*$^{+/+}$ $n = 3$ mice, *CEP250*$^{-/-}$ $n = 3$ mice. At least 50 cells were analyzed in each mouse and the average was calculated for each mouse.

F Schematic diagram showing *CEP250* regulates the position of centrosomes in GSCs during mitosis. In *CEP250*$^{+/+}$ GSCs, centrosome linker keeps the centrosomes relatively close until late prophase, which induces the formation of basal enrichment of E-cadherin. On the one hand, such enrichment might be important in determining the horizontal position of centrosome to facilitate the horizontal division and stem cell maintenance. In addition, basal E-cadherin enrichment helps to position the mother centrosome relatively close to the basement membrane, therefore facilitates the inheritance of mother centrosome by the GSCs. By contrast, such regulation of centrosome positioning is lost in *CEP250*$^{-/-}$ GSCs. Thus, *CEP250*$^{-/-}$ GSCs display randomized spindle orientation and randomly inherit mother or daughter centrosomes.

Data information: In (B), data are presented as mean ± SEM. ****$P < 0.001$ (the Mann–Whitney test). In (E), data are presented as mean ± SEM. ****$P < 0.001$ (the unpaired Student's *t*-test).

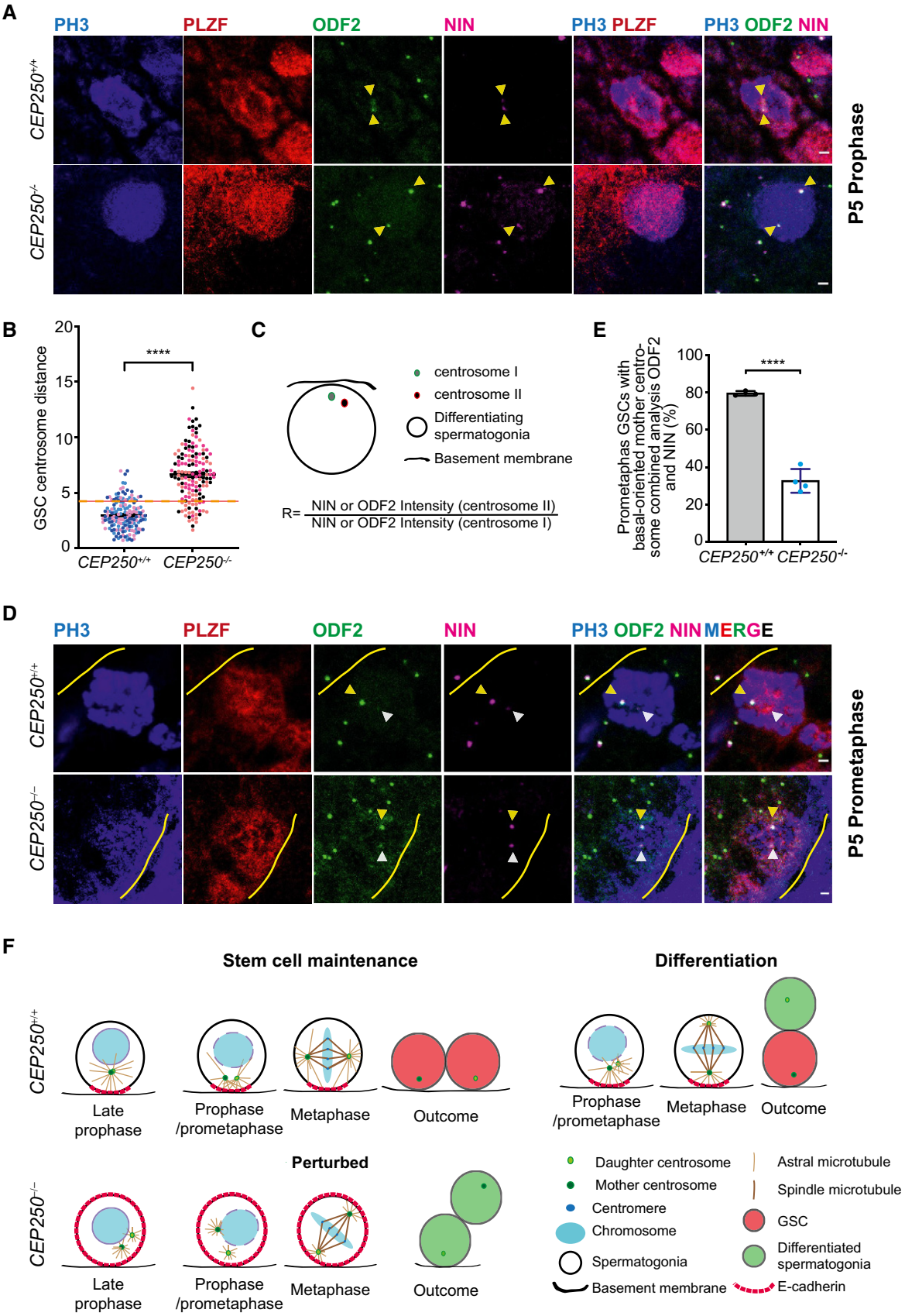

Figure 7.

These findings indicate that in *CEP250*$^{-/-}$ GSCs the change of E-cadherin polarity pattern in prophase is perturbed, which may eventually lead to defects in GSC maintenance.

CEP250$^{-/-}$ GSCs show premature centrosome separation in prophase

In order to gain greater insight into the basis for the striking impact of abolishing centrosome linkage in mitotic GSCs, we examined inter-centrosomal distance in early mitotic GSCs of P5 mice (Figs 7A and B, and EV4A). At prophase, little (around 20%) of the *CEP250*$^{+/+}$ GSCs had an inter-centrosomal distance > 4 μm, which was considered as the centrosome distance threshold to mark cells with well separated centrosomes (Hata *et al*, 2019). By contrast, at the equivalent stage > 80% early mitotic GSCs in *CEP250*$^{-/-}$ mice had achieved centrosome separations greater than > 4 μm (Figs 7A and B, and EV4A). Therefore, the lack of a centrosome linkage leads to greater centrosome separation in GSCs during prophase.

CEP250$^{-/-}$ GSCs showed defects in regulating centrosome position during mitosis

The relative position of mother and daughter centrosomes during mitosis was investigated in P5 GSCs. The centrosome duplicates only once per cell cycle and does so in a semi-conservative manner to form two centrosomes, one of which contains the old mother centriole (i.e., the mother centrosome), while the other receives the new mother centriole (i.e., daughter centrosome; Delattre & Gonczy, 2004). The SDAs of the mother centrosome are in most cases more strongly marked by ODF2 and Ninein (NIN) than at the daughter centrosome (Viol *et al*, 2020). Since ODF2 and NIN antibodies resulted in background signals in the mouse testes, we used double staining approach to ensure that the overlapping ODF2/NIN signals were centrosomes.

While close to 30% of prometaphase *CEP250*$^{+/+}$ GSCs display two centrosomes in a horizontal manner parallel to the basement membrane, this proportion of cells was significantly decreased in *CEP250*$^{-/-}$ GSCs (Fig EV4B and C). We next focused our attention upon the relative proximity of the mother centrosome to the basement membrane during prometaphase (Fig 7C). The mother centrosome was close to the basement membrane in the majority of *CEP250*$^{+/+}$ GSCs, whereas the association between the mother centrosome and the basement membrane was randomized when C-Nap 1 had been removed in *CEP250*$^{-/-}$ GSCs (Figs 7D and E, and EV4D and E). Again, such positioning of mother vs. daughter centrosome was randomized in metaphase *CEP250*$^{-/-}$ GSCs, while it persisted in *CEP250*$^{+/+}$ GSCs (Fig EV5A–D). Thus, the centrosome linker is important for the correct positioning of the mitotic spindle relative to the basal membrane.

Discussion

The integrity of centrosomes is essential for the development in mammals. Loss of function of centrosomal proteins with roles in centrosome organization and maturation, microtubule organization, centrosome-spindle pole connection, or ciliogenesis cause a spectrum of developmental defects in mice from embryonic lethality, heart development defects, microcephaly, dwarfism, and skeletal abnormalities (Chavali *et al*, 2014). Therefore, it was surprising that the absence of the central centrosome linker protein C-Nap1 was not accompanied by any of these phenotypes. Instead, male *CEP250*$^{-/-}$ mice were normal in terms of brain and body weight (Fig 1A–D) but were sterile because the testis did not produce sperms. The lack of any sperm production in *CEP250*$^{-/-}$ mouse testis is distinct from, e.g., Bardet-Biedl syndrome, whereby *BBS4* gene loss leads to immobile sperms that lack the flagellum (Mykytyn *et al*, 2004) nor does such spermatogenic defect in *CEP250*$^{-/-}$ mouse resemble the testis malformation observed in *ASPM1* mutant mice, in which significant number of spermatogenic cells are still present in adult stages (Pulvers *et al*, 2010).

How does loss of the centrosome linker cause sterility? Detailed analysis of male *CEP250*$^{-/-}$ mice indicated strong depletion of germ cells in testis in young mice (9–14 weeks from birth). This defect was not caused by the malfunction of the supporting somatic cells, particularly the Sertoli cells, since they did not display significant change in *CEP250*$^{-/-}$ mice and expression of the Cre recombinase specifically in germ cells of *CEP250*-Flox mice caused comparable phenotypes as observed in whole-body *CEP250*$^{-/-}$ mice. Thus, the sterility in *CEP250*$^{-/-}$ male mice is caused by malfunctions of GSCs.

A link between stem cell maintenance and centrosomes was observed in other organisms and in the mammalian brain. However, no uniform picture of the connection between centrosomes and stem cells has been established. In the mouse brain, the mother centrosome of a neural stem cell is anchored to the apical membrane of the ventricle via a primary cilium, which consequently regulates the behavior and properties of the stem cell (Yamashita *et al*, 2003, 2007; Wang *et al*, 2009; Ortega *et al*, 2019; Shao *et al*, 2020), while in *Drosophila* the male GSCs are attached to the hub cells via adherents junctions, toward which the mother centrosome is oriented. Our study now suggests that mouse GSCs are in terms of asymmetric division closer to *Drosophila* GSCs than to mammalian neural stem cells. Importantly, however, our analysis of *CEP250*$^{-/-}$ GSCs uncovered three novel principals that regulate GSC maintenance in male testis (Fig 7F). First, our data suggest that the closeness of the centrosomes provided by the centrosome linker until G2/early mitosis was required to induce an E-cadherin polarity mark toward the basal membrane role, which may have a determinant role in spindle orientation and cell fate decision in the GSCs. Second, we propose that two close together centrosomes are more efficient in inducing the E-cadherin polarity mark than a single centrosome. These data together suggest signaling from the centrosomes to the basal membrane. We speculate that mitotic kinases or other signaling molecules at centrosomes send a signal to the cell cortex that is stronger when the two centrosomes are closed together (Cowan & Hyman, 2004; Bondaz *et al*, 2019) (Kapoor & Kotak, 2020; Gan & Motegi, 2021). Finally, the temporally established E-cadherin polarity mark can in turn direct the correct positioning of the centrosomes and mitotic spindle, which is essential in determining cell division plane and daughter cell fate. We speculate that during early GSC development, the basal-polarized E-cadherin may regulate the position of the two centrosomes during mitosis to keep them in a parallel position relative to the basement membrane, thus helping to establish a horizontally positioned mitotic spindle. Such regulation will support the self-proliferation of the GSCs by ensuring their parallel division, hence helping the maintenance of the stem cell pool. As a result, failure of centrosome cohesion and polarity establishment as is the

case in the testis of *CEP250*$^{-/-}$ mice results in randomization of the mitotic spindle that is not as directed as in WT GSCs. This can cause GSCs to develop prematurely into SCP1 positive spermatogonia.

In addition, our study uncovers that later in development, the basal-polarized E-cadherin also support stem cell maintenance through ensuring the correct inheritance of the older mother centrosome. We speculate that E-cadherin may contribute to the regulation of stem cell maintenance versus differentiation via keeping the mother centrosome at a relatively close proximity to the basement membrane in mitosis. This facilitates the inheritance of the older mother centrosome to the daughter cell that remains at the basement membrane after GSC cells have divided, which will remain the stem cell.

The link between centrosome position and the E-cadherin mark at the cell membrane may be provided by astral microtubules organized by the centrosomes. The older mother centrosome may organize more astral microtubules or, as this is the case for the mother yeast spindle pole body (SPB), the functional equivalent of the mammalian centrosome. The mother SPB specifically loads the protein Kar9 that interacts with Myo2 at the cell membrane onto astral microtubules (Yin *et al*, 2000; Liakopoulos *et al*, 2003; Maekawa *et al*, 2003). Alternatively, the older mother centrosome may associate with microtubule-attached proteins that interact with cell cortex factors. In a study concerning culture MDCK cells, a connection with the centrosome was laid via an interaction of E-cadherin with the LGN/Numa complex (Gloerich *et al*, 2017) that functions through cortical pulling forces exerted on astral microtubules during mitosis (Gonczy, 2008). Nevertheless, the association between the centrosome and cell cortex factors remains to be uncovered in mice.

The failure to orient the mitotic spindle in a defined way disrupts the spatial temporal organization of spermatogenic cells in *CEP250*$^{-/-}$ mice. PLZF-positive GSCs that initially localize to the basement membrane and translocate into the supra-basal localization of seminiferous tubules when they differentiate and express SCP1 marker, were found prematurely in the lumen of the seminiferous tubules in *CEP250*$^{-/-}$ mice. This defect probably induces apoptosis, which likely eliminates the SCP1-positive cells that prematurely translocated toward the center of the seminiferous tubules, as our data indicate higher percentage of apoptotic germ cells were already present at P5 *CEP250*$^{-/-}$ testis (Fig 2G and I). One possible explanation is that germ cell development and survival rely on the somatic niche, and the regulating factors they secrete (Griswold, 2016). Thus, the premature translocation and misorientation of the GSCs may result in elimination of these cells in *CEP250*$^{-/-}$ testis. Notably, *CEP250*$^{-/-}$ germ cells displayed more substantial increase of apoptosis between P10 and P14 (Fig 2G and I), the timing when the first round of meiosis starts, which indicates an additional defect contributing to germ cell loss during this time. This notion was further supported by the finding that *CEP250*$^{-/-}$ spermatocytes were unable to proceed till zygotene and diplotene stage and a proportion of them display a dysregulated form with aberrant γH2AX pattern (Appendix Fig S5A and B), which may trigger meiotic arrest and elimination of these defective cells. During revision of our manuscript, a study of *CEP250*$^{-/-}$ mouse was published specifically focusing on the meiotic defect of *CEP250*$^{-/-}$ spermatocytes (Floriot *et al*, 2021), confirming our finding on a defective meiosis in the testis of *CEP250*$^{-/-}$ mice.

Why does the defect in *CEP250*$^{-/-}$ mice relative specifically affect GSCs? Presently we cannot exclude defects in other tissues than testis, due to lack of in-depth histological analysis. However, it is possible that the mechanism of centrosome induced E-cadherin polarity might be specific for testis, as E-cadherin seems to be an explicit cell surface marker for GSCs in mice (Tolkunova *et al*, 2009). Alternatively, redundant centrosome cohesion pathways that vary in their activities in different tissues may compensate each other depending on their expression profiles. Indeed, a microtubule and KIFC3 motor dependent centrosome cohesion mechanism has been described that has the ability to compensate for the loss of C-Nap1-dependent centrosome cohesion (Hata *et al*, 2019).

Materials and Methods

Animals

Mice carrying allele *CEP250tm1a*$^{(EUCOMM)Wtsi}$ were purchased from Wellcome Trust Sanger Institute. Mice were back-crossed 5 times to C57BL/6J and bred in house. Mice were bred and crossed in house with C57BL/6N-Tg (CMV) and C57BL/6.FVB-Tg (Stra8-icre) mice to generate *CEP250*$^{-/-}$ and *CEP250*$^{flox/flox}$*/Stra8-Cre* mice, respectively. All experiments involving animals were reviewed and approved by the Heidelberg University Animal Care and Use Ethical Committee and Regierungspräsidium Karlsruhe (Animal Project: T-46/19). Animals were housed and bred according to institutional guidelines.

MEF

Mouse embryonic fibroblasts were isolated in house from *CEP250*$^{+/+}$ and *CEP250*$^{-/-}$ mouse embryos at E13.5 as described (Jozefczuk *et al*, 2012). In brief, a timed pregnant female was euthanized at E13.5, from which embryos were dissected from the uterus. In a sterile environment, the placenta and surrounding tissues were removed. The head and embryonic organs were subsequently removed. The remaining tissues were homogenized on ice and subsequently digested by trypsinization (0.05% trypsin–EDTA) (Gibco, Invitrogen), including 100 Kunitz units of DNase I (Biolabs) per embryo to isolate the fibroblasts. Cells were cultured in DMEM supplemented with 10% FBS, 2 mM L-glutamine, and 1% penicillin–streptomycin in 37°C environment supplemented with 5% CO_2. The cultured MEFs were used immediately within passage 0–2 for analysis.

Fertility assays

Mating of 9- to 14-week-old mice was used in the quantification of litter size. *CEP250*$^{+/+}$ male and *CEP250*$^{+/+}$ female (19 mating pairs and 141 offsprings), *CEP250*$^{-/-}$ male and *CEP250*$^{+/+}$ female (9 mating pairs and 0 offsprings), and *CEP250*$^{+/+}$ male and *CEP250*$^{-/-}$ female (12 mating pairs and 44 offsprings) were analyzed.

Histopathology

Mice were euthanized by cervical dislocation. Tissue samples from representative organs were collected and fixed in 4% paraformaldehyde (PFA) at 4°C for 24 h. The tissues were subsequently transferred to PBS solution and handed over to Prof. Hermann-Josef Gröne (DKFZ, Pathology Department) for histopathologic analysis.

Briefly, the tissues were paraffin embedded and processed for hematoxylin and eosin (H & E) staining. The stained sections were analyzed in collaboration with Prof. Hermann-Josef Gröne.

Viable sperm isolation

Adult mice (9- to 14-week-old) were euthanized with cervical dislocation. Sperm cells were subsequently isolated from the dead male mice, following the method described by Duselis and Vrana (2007). In brief, caudal epididymis were isolated from 9- to 14-week-old mice and placed in 9% milk solution. The caudal epididymis was cut open using a gauge needle. The sperms were squeezed out from the open caudal epididymis and collected for evaluation under the microscope. The number of sperms isolated per testis was estimated by using a hemocytometer.

Immunofluorescence on tissue sections

Tissue samples were dissected and washed in PBS. For immunofluorescence of non-centrosome proteins, the dissected tissue samples were fixed in 4% paraformaldehyde overnight at 4°C, and immerged in PBS. The tissue samples were subsequently embedded in Tissue-Tek O.C.T. TM Compound (Sakura 4583). The tissue sample blocks were subsequently stored at −80°C. Sections of 10 μm were made using Leica 1950 cryostat and stored at −80°C. The sections were recovered at room temperature (RT), washed in PBS for 5 min at RT, permeabilized in 0.5% Triton X-100 in PBS for 15 min, and washed in PBS for 5 min at RT. For immunofluorescence of centrosome proteins, the dissected tissue samples were immediately embedded in Tissue-Tek O.C.T. TM Compound (Sakura 4583) over liquid nitrogen following dissection. The tissue sample blocks were subsequently stored at −80°C. Sections of 10 μm were made using Leica 1950 cryostat and stored at −80°C. The tissue sections were fixed in methanol at −20°C for 30 min and washed in PBS for 5 min. For immunofluorescence staining, the prepared sections were incubated in blocking solution (3% BSA, 0.1% Triton X-100) for 1 h at RT, following overnight incubation of primary antibody (diluted in 1% BSA, 0.05% Triton X-100) at 4°C. The sections were washed by 10-min incubation in PBS for 3 times and subsequently incubated with secondary antibodies (diluted 1:500 in 1% BSA, 0.05% Triton X-100) at RT for 1 h. DNA was stained with Hoechst 33342 (0.2 g/ml, Calbiochem) diluted 1:3,000 in PBS for 10 min and mounted with Mowiol (Calbiochem) with or without PPD (Sigma). The following primary antibodies were used: anti-MVH (rabbit, 1:3,000, ab13840, Abcam), anti-GATA4 (rabbit, 1:400, ab84593, Abcam), anti-PLZF (goat, 1:100, AF2944, R&D Systems), anti-SCP1 (rabbit, 1:300, ab15090, Abcam), anti-γ-Tubulin (mouse, 1:500, ab27074, Abcam), anti-PH3 (rabbit, 1:3,000, #3377, Cell Signalling Technology), anti-PH3 (mouse, 1:100, #9706, Cell Signalling Technology), anti-E-cadherin (rabbit, 1:200, #3195, Cell Signalling Technology), anti-ODF2 (Guinea pig, 1:500, a gift from Pereira lab; Kuhns *et al*, 2013), anti-Ninein-L79 (rabbit, 1:600, a gift from M. Bornens Lab), anti-C-Nap1 (rabbit, 1:250, 14498-1-AP, Proteintech), and anti-C-CASP3 (rabbit, 1:250, #9579, Cell Signalling). The following secondary antibodies were used: donkey-anti-rabbit IgG (H + L) conjugated to Alexa Fluor 488 or Alexa Fluor 647 (A31573/A21206, Life Technologies), donkey-anti-mouse IgG (H + L) conjugated to Alexa Fluor 488 (A21202, Life Technologies), goat-anti-mouse IgG (H + L) conjugated to Alexa Fluor 405 (A31553, Life Technologies), goat-anti-guinea pig IgG (H + L) conjugated to Alexa Fluor 488 (A11073, Life Technologies), and donkey-anti-goat IgG (H + L) conjugated to Alexa Fluor 555 (A21432, Life Technologies).

Spindle orientation analysis

Mouse testis were dissected and processed according to (see "Immunofluorescence on tissue sections"). The sections were labeled with anti-PH3, anti-γ-Tubulin, anti-PLZF to visualize the mitotic chromosomes, centrosomes, and germ stem cells, respectively (see "Immunofluorescence on tissue sections"). Z-stack images were acquired with Leica TCS SP5 confocal microscope with the top and lower panel spanning the top and bottom of the cell and 1 μm interval between each stack. The images were imported in Fiji for analysis. Z-stacks were displayed as 2D maximum projections. The spermatogonia in metaphase or anaphase were used to determine the cell spindle axis, for which a line was drawn bisecting the two centrosomes (Fig 5 A and B, Appendix Fig S6A and B). The basement membrane plane was determined by drawing a line parallel to the basement membrane on the point where the basement membrane and spermatogonium contacted (Fig 5A and B, Appendix Fig S6A and B). The spindle angle Ø was calculated between the cell spindle axis and the basement membrane plane (Fig 5A and B, Appendix Fig S6A and B).

Asymmetric centrosome position analysis

Mouse testis was dissected and processed according to "Immunofluorescence on tissue sections". The sections were labeled with anti-PH3 for mitotic chromosomes, anti-PLZF for germ stem cells, anti-ODF2, and anti-Ninein for centrosomes (see Immunofluorescence on tissue sections). Z-stack images were acquired with Leica TCS SP5 confocal microscope, with the top and lower panel spanning the top and bottom of the cell and 1-μm interval between each stack. The images were imported in Fiji for analysis. Fluorescence intensity quantifications were obtained from sum projections of Z-stacks. The intensity of ODF2 and NIN in a mitotic spermatogonium was measure, and the intensity ratio R between the two centrosomes was calculated as centrosome closer to the basement membrane/centrosome further from the basement membrane (Figs 7C–E and EV5B–D). A threshold of 15% difference was drawn. Given the ratio is smaller than 85%, the mother centrosome was considered to be preferentially placed close to the basement membrane. Given the ratio is larger than 115%, the daughter centrosome was considered to be preferentially placed close to the basement membrane.

Cultured cell treatments and immunofluorescence

Mouse embryonic fibroblast cells were cultured in DMEM supplemented with 10% FBS, 2 mM L-glutamine and 1% penicillin-streptomycin in 37°C environment with 5% CO_2. The cultured MEFs were used immediately within passage 0–2 for analysis. The cells were seeded on a coverslip. Microtubule depolymerization was performed using nocodazole at 5 μM for 1 h. For immunofluorescence, the cells were fixed at −20°C for 10 min. The samples were incubated in blocking solution (3% BSA, 0.1% Triton X-100)

for 1 h at RT, following overnight incubation of primary antibody (diluted in 1% BSA, 0.05% Triton X-100) at 4°C. The coverslips were washed by 10-min incubation in PBS for 3 times and subsequently incubated with secondary antibodies (diluted 1:500 in 1% BSA, 0.05% Triton X-100) at RT for 1 h. DNA was stained with Hoechst 33342 (0.2 g/ml, Calbiochem) diluted 1:3,000 in PBS for 5 min and mounted with Mowiol (Calbiochem) with or without PPD (Sigma). The following primary antibodies were used: anti-C-Nap1 (rabbit, 1:500, 14498-1-AP, Proteintech), and anti-γ-Tubulin (mouse, 1:500, ab27074, Abcam). The following secondary antibodies were used: donkey-anti-rabbit IgG (H + L) conjugated to Alexa Fluor 555 (A32794, Life Technologies) and donkey-anti-mouse IgG (H + L) conjugated to Alexa Fluor 488 (A21202, Life Technologies).

Microscopy

Immunofluorescence images were acquired on Leica TCS SP5 confocal microscope, using x40 and x63 objectives and LAS AF SP5 software (Figs 1O, 2G, 3C, 4B, 5A and B, 6A–D, 7A and D, EV2C and G, EV3A, C and E, EV4B, EV5A, Appendix Fig S1L, S3G and H, S4A, S5A and B, S6A and B) or on Olympus Xcellence microscope IX81, using 10× and 20× objectives and Olympus Xcellence software (Figs 1M, 2D, 3A, EV1F, I and J, Appendix Fig S3G and H). Bright-field images were acquired on Olympus BX60 microscope using ×10 and ×20 objectives and ImageJ software (Fig 1I–K and Appendix Fig S1A–H) or stereoscope OLYMPUS SZX7 using 0.8×, 1×, 2×, 3.2×, and 5× objectives (Figs 1C and F, 2A, EV2A, Appendix Fig S1J and S3A–D). The images were imported in Fiji for analysis. Z-stacks were displayed as 2D maximum projections. For fluorescence intensity measurement (Figs 7D, EV4D and E, and EV5A), intensity profiles were obtained from sum projections of *Z*-stacks.

Immunoblotting

Proteins were separated on 6% SDS–PAGE gel and transferred to a PVDF membrane using a Bio-Rad Mini-Transblot Electrophoretic Transfer System. Membranes were blocked with 5% milk in TBST and probed with primary antibodies C-Nap1 (rabbit, 1:300, 14498-1-AP, Proteintech), Lamin B1 (rabbit, 1:1,000, ab16048 Abcam) diluted in 3% BSA in TBST. The membrane was subsequently blocked with HRP-conjugated secondary antibodies, anti-rabbit IgG (H + L) (donkey, 1:3,000, 711-035-152, Jackson) diluted in 5% milk TBST at RT for 1 h.

PCR-based genotyping

Mouse biopsies were digested by 4 h incubation with 1 mg/ml Proteinase K (Sigma) in lysis butter (100 mM Tris–Cl, 0.2% SDS, 200 mM NaCl and 5 mM EDTA, pH 8.5), followed by 10-min inactivation at 95°C and 2:15 dilution in deionized water. The samples are directly used as PCR templates. The primers used are indicated as below, *CEP250*-Flox Fwd: GCAGGAGGACGTGGAAAAAC, *CEP250*-Flox Rv: AACCCAGCAAAGGTTCAGG, *CEP250* del Fwd: CAAGGCG CATAACGATACCAC, *CEP250* del Rv: GAGAGCCCGAGCCATGA TAA, CMV-Cre Fwd: GAACCTGATGGACATGTTCAGG, MV-Cre Rv: AGTGCGTTCGAACGCTAGAGCCTGT.

Statistics

For mouse experiments, n represents the number of independent biological replicates. A minimum of three biological replicates was performed. Power calculation was done to determine the size of animals according to method described in (Charan & Kantharia, 2013). Complied data are expressed as ± SEM. For statistical comparison between two conditions with representative or averaged values of each biological replicate, the unpaired Student's *t* test was applied (Figs 1B, D, G, H, L and O, 2C, 5E and F, 6C, E and G, 7B and E, EV2B, E and F, EV3B, D and F, EV4C; Appendix Fig S1K and M, S2A and B, S3E and I, S4B; Appendix Fig S6E and F). For statistical comparison between two conditions with individual values of each measured parameters for all biological replicates, the Mann-Whitney test was applied (Figs 2E, F, H and I; 3B and E–H; 4C–E, EV1G and H, EV2D, EV4A, and Appendix Fig S4C). The level of significance was indicated as follows: n.s., not significant, $*P < 0.05$, $**P < 0.01$, $***P < 0.005$, $****P < 0.001$.

Data availability

This study includes no data deposited in external repositories.

Expanded View for this article is available online.

Acknowledgements

We thank H.J. Gröne for his excellent knowledge and assistance in the histopathological analysis. The ODF2 and Ninein (L79) antibodies were kindly provided by G. Pereira and M. Bornens. The CMV-Cre mice were kindly provided by H. Monyer. We thank C. Scholl and S. Hata for the technical assistance and discussion and G. Pereira and I. Hagan for comments to the manuscript. The work of E.S. is supported by a grant of the Deutsche Forschungsgemeinschaft (DFG) (Schi 295/6-2). Open Access funding enabled and organized by Projekt DEAL.

Author contributions

Elmar Schiebel: Conceptualization; Supervision; Funding acquisition; Writing—original draft. **Hairuo Dang:** Conceptualization; Data curation; Formal analysis; Investigation; Methodology; Writing—original draft. **Ana Martin-Villalba:** Methodology; Writing—review and editing.

In addition to the CRediT author contributions listed above, the contributions in detail are:

HD and ES conceived and designed experiments. AM-V contributed to supervision of the study. HD performed experiments. HD analyzed the data. HD and ES wrote the manuscript. ES supervised the study and acquired for funding.

Disclosure and competing interests statement

The authors declare that they have no conflict of interest.

References

Anderson EL, Baltus AE, Roepers-Gajadien HL, Hassold TJ, de Rooij DG, van Pelt AM, Page DC (2008) Stra8 and its inducer, retinoic acid, regulate meiotic initiation in both spermatogenesis and oogenesis in mice. *Proc Natl Acad Sci* 105: 14976 – 14980

Bahe S, Stierhof YD, Wilkinson CJ, Leiss F, Nigg EA (2005) Rootletin forms centriole-associated filaments and functions in centrosome cohesion. *J Cell Biol* 171: 27 – 33

Bolcun-Filas E, Costa Y, Speed R, Taggart M, Benavente R, De Rooij DG, Cooke HJ (2007) SYCE2 is required for synaptonemal complex assembly, double strand break repair, and homologous recombination. *J Cell Biol* 176: 741 – 747

Bondaz A, Cirillo L, Meraldi P, Gotta M (2019) Cell polarity-dependent centrosome separation in the *C. elegans* embryo. *J Cell Biol* 218: 4112 – 4126

Bornens M (2002) Centrosome composition and microtubule anchoring mechanisms. *Curr Opin Cell Biol* 14: 25 – 34

Camargo Ortega G, Falk S, Johansson PA, Peyre E, Broix L, Sahu SK, Hirst W, Schlichthaerle T, De Juan Romero C, Draganova K *et al* (2019) The centrosome protein AKNA regulates neurogenesis via microtubule organization. *Nature* 567: 113 – 117

Chan JY (2011) A Clinical Overview of Centrosome Amplification in Human Cancers. *Int J Biol Sci* 7: 1122 – 1144

Charan J, Kantharia ND (2013) How to calculate sample size in animal studies? *J Pharmacol Pharmacother* 4: 303 – 306

Chavali PL, Putz M, Gergely F (2014) Small organelle, big responsibility: the role of centrosomes in development and disease. *Philos Trans R Soc Lond B Biol Sci* 369: 20130468

Chen SR, Tang JX, Cheng JM, Li J, Jin C, Li XY, Deng SL, Zhang Y, Wang XX, Liu YX (2015) Loss of Gata4 in Sertoli cells impairs the spermatogonial stem cell niche and causes germ cell exhaustion by attenuating chemokine signaling. *Oncotarget* 6: 37012 – 37027

Conduit PT, Wainman A, Raff JW (2015) Centrosome function and assembly in animal cells. *Nat Rev Mol Cell Biol* 16: 611 – 624

Costoya JA, Hobbs RM, Barna M, Cattoretti G, Manova K, Sukhwani M, Orwig KE, Wolgemuth DJ, Pandolfi PP (2004) Essential role of Plzf in maintenance of spermatogonial stem cells. *Nat Genet* 36: 653 – 659

Cowan CR, Hyman AA (2004) Centrosomes direct cell polarity independently of microtubule assembly in C-elegans embryos. *Nature* 431: 92 – 96

Delattre M, Gonczy P (2004) The arithmetic of centrosome biogenesis. *J Cell Sci* 117: 1619 – 1629

Delgehyr N, Sillibourne J, Bornens M (2005) Microtubule nucleation and anchoring at the centrosome are independent processes linked by ninein function. *J Cell Sci* 118: 1565 – 1575

Di Carlo A, Travia G, De Felici M (2000) The meiotic specific synaptonemal complex protein SCP3 is expressed by female and male primordial germ cells of the mouse embryo. *Int J Dev Biol* 44: 241 – 244

Dumont NA, Wang YX, von Maltzahn J, Pasut A, Bentzinger CF, Brun CE, Rudnicki MA (2015) Dystrophin expression in muscle stem cells regulates their polarity and asymmetric division. *Nat Med* 21: 1455 – 1463

Duselis AR, Vrana PB (2007) Harvesting sperm and artificial insemination of mice. *J vis Exp* 3: 184

Fabbri L, Bost F, Mazure NM (2019) Primary cilium in cancer hallmarks. *Int J Mol Sci* 20: 1336

Floriot S, Bellutti L, Castille J, Moison P, Messiaen S, Passet B, Boulanger L, Boukadiri A, Tourpin S, Beauvallet C *et al* (2021) CEP250 is required for maintaining centrosome cohesion in the germline and fertility in male mice. *Front Cell Dev Biol* 9: 754054

Floriot S, Vesque C, Rodriguez S, Bourgain-Guglielmetti F, Karaiskou A, Gautier M, Duchesne A, Barbey S, Fritz S, Vasilescu A *et al* (2015) C-Nap1 mutation affects centriole cohesion and is associated with a Seckel-like syndrome in cattle. *Nat Commun* 6: 6894

Fry AM, Mayor T, Meraldi P, Stierhof YD, Tanaka K, Nigg EA (1998) C-Nap1, a novel centrosomal coiled-coil protein and candidate substrate of the cell cycle-regulated protein kinase Nek2. *J Cell Biol* 141: 1563 – 1574

Gai M, Bianchi FT, Vagnoni C, Vernì F, Bonaccorsi S, Pasquero S, Berto GE, Sgrò F, Chiotto AM, Annaratone L *et al* (2016) ASPM and CITK regulate spindle orientation by affecting the dynamics of astral microtubules. *EMBO Rep* 17: 1396 – 1409

Gan WJ, Motegi F (2021) Mechanochemical control of symmetry breaking in the *Caenorhabditis elegans* zygote. *Front Cell Dev Biol* 8: 619869

Gloerich M, Bianchini JM, Siemers KA, Cohen DJ, Nelson WJ (2017) Cell division orientation is coupled to cell-cell adhesion by the E-cadherin/LGN complex. *Nat Commun* 8: 13996

Gonczy P (2008) Mechanisms of asymmetric cell division: flies and worms pave the way. *Nat Rev Mol Cell Biol* 9: 355 – 366

Graser S, Stierhof YD, Nigg EA (2007) Cep68 and Cep215 (Cdk5rap2) are required for centrosome cohesion. *J Cell Sci* 120: 4321 – 4331

Griswold MD (1998) The central role of Sertoli cells in spermatogenesis. *Semin Cell Dev Biol* 9: 411 – 416

Griswold MD (2016) Spermatogenesis: the commitment to meiosis. *Physiol Rev* 96: 1 – 17

Hata S, Peidro AP, Panic M, Liu P, Atorino E, Funaya C, Jakle U, Pereira G, Schiebel E (2019) The balance between KIFC3 and EG5 tetrameric kinesins controls the onset of mitotic spindle assembly. *Nat Cell Biol* 21: 1138 – 1151

Hehnly H, Canton D, Bucko P, Langeberg LK, Ogier L, Gelman I, Santana LF, Wordeman L, Scott JD (2015) A mitotic kinase scaffold depleted in testicular seminomas impacts spindle orientation in germ line stem cells. *Elife* 4: e09384

Hoja MR, Liu JG, Mohammadieh M, Kvist U, Yuan L (2004) E2F1 deficiency impairs murine spermatogenesis and augments testicular degeneration in SCP3-nullizygous mice. *Cell Death Differ* 11: 354 – 356

Jenkins AB, McCaffery JM, Van Doren M (2003) Drosophila E-cadherin is essential for proper germ cell-soma interaction during gonad morphogenesis. *Development* 130: 4417 – 4426

Jozefczuk J, Drews K, Adjaye J (2012) Preparation of mouse embryonic fibroblast cells suitable for culturing human embryonic and induced pluripotent stem cells. *J vis Exp* 64: 3854

Kapoor S, Kotak S (2020) Centrosome Aurora A gradient ensures single polarity axis in *C. elegans* embryos. *Biochem Soc Trans* 48: 1243 – 1253

Kiyomitsu T, Cheeseman IM (2013) Cortical dynein and asymmetric membrane elongation coordinately position the spindle in anaphase. *Cell* 154: 1401

Kuhns S, Schmidt KN, Reymann J, Gilbert DF, Neuner A, Hub B, Carvalho R, Wiedemann P, Zentgraf H, Erfle H *et al* (2013) The microtubule affinity regulating kinase MARK4 promotes axoneme extension during early ciliogenesis. *J Cell Biol* 200: 505 – 522

Lagos-Cabré R, Moreno RD (2008) Mitotic, but not meiotic, oriented cell divisions in rat spermatogenesis. *Reproduction* 135: 471 – 478

Lens SMA, Medema RH (2019) Cytokinesis defects and cancer. *Nat Rev Cancer* 19: 32 – 45

Li H, Frappart L, Moll J, Winkler A, Kroll T, Hamann J, Kufferath I, Groth M, Taudien S, Schütte M *et al* (2016) Impaired planar germ cell division in the testis, caused by dissociation of RHAMM from the spindle, results in hypofertility and seminoma. *Can Res* 76: 6382 – 6395

Liakopoulos D, Kusch J, Grava S, Vogel J, Barral Y (2003) Asymmetric loading of Kar9 onto spindle poles and microtubules ensures proper spindle alignment. *Cell* 112: 561 – 574

Lovelace DL, Gao Z, Mutoji K, Song YC, Ruan JH, Hermann BP (2016) The regulatory repertoire of PLZF and SALL4 in undifferentiated spermatogonia. *Development* 143: 1893 – 1906

Maekawa H, Usui T, Knop M, Schiebel E (2003) Yeast Cdk1 translocates to the plus end of cytoplasmic microtubules to regulate bud cortex interactions. *EMBO J* 22: 438 – 449

Mahadevaiah SK, Turner JMA, Baudat F, Rogakou EP, de Boer P, Blanco-Rodriguez J, Jasin M, Keeney S, Bonner WM, Burgoyne PS (2001) Recombinational DNA double-strand breaks in mice precede synapsis. *Nat Genet* 27: 271 – 276

Martin-Belmonte F, Perez-Moreno M (2012) Epithelial cell polarity, stem cells and cancer. *Nat Rev Cancer* 12: 23 – 38

McClellan KA, Gosden R, Taketo T (2003) Continuous loss of oocytes throughout meiotic prophase in the normal mouse ovary. *Dev Biol* 258: 334 – 348

Mykytyn K, Mullins RF, Andrews M, Chiang AP, Swiderski RE, Yang B, Braun T, Casavant T, Stone EM, Sheffield VC (2004) Bardet-Biedl syndrome type 4 (BBS4)-null mice implicate Bbs4 in flagella formation but not global cilia assembly. *Proc Natl Acad Sci USA* 101: 8664 – 8669

Nechipurenko IV, Olivier-Mason A, Kazatskaya A, Kennedy J, McLachlan IG, Heiman MG, Blacque OE, Sengupta P (2016) A conserved role for girdin in basal body positioning and ciliogenesis. *Dev Cell* 38: 493 – 506

Neumüller RA, Knoblich JA (2009) Dividing cellular asymmetry: asymmetric cell division and its implications for stem cells and cancer. *Genes Dev* 23: 2675 – 2699

Nigg EA, Holland AJ (2018) Once and only once: mechanisms of centriole duplication and their deregulation in disease. *Nat Rev Mol Cell Biol* 19: 297 – 312

Oatley JM, Brinster RL (2012) The germline stem cell niche unit in mammalian testes. *Physiol Rev* 92: 577 – 595

Panic M, Hata S, Neuner A, Schiebel E (2015) The centrosomal linker and microtubules provide dual levels of spatial coordination of centrosomes. *PLoS Genet* 11: e1005243

Paridaen J, Wilsch-Brauninger M, Huttner WB (2013) Asymmetric inheritance of centrosome-associated primary cilium membrane directs ciliogenesis after cell division. *Cell* 155: 333 – 344

Pulvers JN, Bryk J, Fish JL, Wilsch-Brauninger M, Arai Y, Schreier D, Naumann R, Helppi J, Habermann B, Vogt J *et al* (2010) Mutations in mouse Aspm (abnormal spindle-like microcephaly associated) cause not only microcephaly but also major defects in the germline. *Proc Natl Acad Sci USA* 107: 16595 – 16600

Remo A, Li X, Schiebel E, Pancione M (2020) The centrosome linker and its role in cancer and genetic disorders. *Trends Mol Med* 26: 380 – 393

de Rooij DG (2017) The nature and dynamics of spermatogonial stem cells. *Development* 144: 3022 – 3030

Saitou M, Yamaji M (2012) Primordial germ cells in mice. *Cold Spring Harb Perspect Biol* 4: a008375

Shaheen R, Jiang N, Alzahrani F, Ewida N, Al-Sheddi T, Alobeid E, Musaev D, Stanley V, Hashem M, Ibrahim N *et al* (2019) Bi-allelic mutations in FAM149B1 cause abnormal primary cilium and a range of ciliopathy phenotypes in humans. *Am J Hum Genet* 104: 731 – 737

Shao W, Yang J, He M, Yu X-Y, Lee CH, Yang Z, Joyner AL, Anderson KV, Zhang J, Tsou M-F *et al* (2020) Centrosome anchoring regulates progenitor properties and cortical formation. *Nature* 580: 106 – 112

Song KK, Ma WW, Huang C, Ding JH, Cui DD, Zhang MM (2016) Expression pattern of mouse vasa homologue (MVH) in the ovaries of C57BL/6 female mice. *Med Sci Monit* 22: 2656 – 2663

Tanaka SS, Toyooka Y, Akasu R, Katoh-Fukui Y, Nakahara Y, Suzuki R, Yokoyama M, Noce T (2000) The mouse homolog of *Drosophila* Vasa is required for the development of male germ cells. *Genes Dev* 14: 841 – 853

Tanos BE, Yang HJ, Soni R, Wang WJ, Macaluso FP, Asara JM, Tsou MFB (2013) Centriole distal appendages promote membrane docking, leading to cilia initiation. *Genes Dev* 27: 163 – 168

Tolkunova EN, Malashicheva AB, Chikhirzhina EV, Kostyleva EI, Zeng W, Luo J, Dobrinskiĭ I, Hierholzer A, Kemler R, Tomilin AN (2009) E-cadherin as a novel surface marker of spermatogonial stem cells. *Tsitologiia* 51: 212 – 218

Tsou MFB, Stearns T (2006) Mechanism limiting centrosome duplication to once per cell cycle. *Nature* 442: 947 – 951

Tsukita S, Katsuno T, Yamazaki Y, Umeda K, Tamura A, Tsukita S (2009) Roles of ZO-1 and ZO-2 in establishment of the belt-like adherens and tight junctions with paracellular permselective barrier function. *Ann NY Acad Sci* 1165: 44 – 52

Turner JMA, Aprelikova O, Xu XL, Wang RH, Kim SS, Chandramouli GVR, Barrett JC, Burgoyne PS, Deng CX (2004) BRCA1, histone H2AX phosphorylation, and male meiotic sex chromosome inactivation. *Curr Biol* 14: 2135 – 2142

Vargas-Hurtado D, Brault JB, Piolot T, Leconte L, Da Silva N, Pennetier C, Baffet A, Marthiens V, Basto R (2019) Differences in mitotic spindle architecture in mammalian neural stem cells influence mitotic accuracy during brain development. *Curr Biol* 29: 2993 – 3005

Viol L, Hata S, Pastor-Peidro A, Neuner A, Murke F, Wuchter P, Ho AD, Giebel B, Pereira G (2020) Nek2 kinase displaces distal appendages from the mother centriole prior to mitosis. *J Cell Biol* 219

de Vries FAT, de Boer E, van den Bosch M, Baarends WM, Ooms M, Yuan L, Liu JG, van Zeeland AA, Heyting C, Pastink A (2005) Mouse Sycp1 functions in synaptonemal complex assembly, meiotic recombination., and XY body formation. *Genes Dev* 19: 1376 – 1389

Wang XQ, Tsai JW, Imai JH, Lian WN, Vallee RB, Shi SH (2009) Asymmetric centrosome inheritance maintains neural progenitors in the neocortex. *Nature* 461: 947 – U206

Yamashita YM, Jones DL, Fuller MT (2003) Orientation of asymmetric stem cell division by the APC tumor suppressor and centrosome. *Science* 301: 1547 – 1550

Yamashita YM, Mahowald AP, Perlin JR, Fuller MT (2007) Asymmetric inheritance of mother versus daughter centrosome in stem cell division. *Science* 315: 518 – 521

Yin HW, Pruyne D, Huffaker TC, Bretscher A (2000) Myosin V orientates the mitotic spindle in yeast. *Nature* 406: 1013 – 1015

Yokonishi T, McKey J, Ide S, Capel B (2020) Sertoli cell ablation and replacement of the spermatogonial niche in mouse. *Nat Commun* 11: 40